Observed Pathways and Interannual Variability of the Warm Inflow Onto the Continental Shelf in the Southern Weddell Sea

Nadine Steiger, Jean-Baptiste Sallée, Elin Darelius, Markus Janout, Svein Østerhus

To cite this version:

Nadine Steiger, Jean-Baptiste Sallée, Elin Darelius, Markus Janout, Svein Østerhus. Observed Pathways and Interannual Variability of the Warm Inflow Onto the Continental Shelf in the Southern Weddell Sea. Journal of Geophysical Research. Oceans, 2024, 129 (11), ⟨10.1029/2023jc020700⟩. ⟨hal-04943830⟩

HAL Id: hal-04943830
https://hal.science/hal-04943830v1

Submitted on 21 Mar 2025

JGR Oceans

RESEARCH ARTICLE

10.1029/2023JC020700

Key Points:

- Extensive network of moorings show the propagation of modified Warm Deep Water from the continental slope into the Filchner Trough
- Anomalously warm inflow in 2017 and 2018 is observed along the whole inflow pathway
- Anomalies were driven by low sea ice concentration and local upwelling above the continental slope

Correspondence to:

J. B. Sallée,
jbsallee@gmail.com

Citation:

Steiger, N., Sallée, J. B., Darelius, E., Janout, M., & Østerhus, S. (2024). Observed pathways and interannual variability of the warm inflow onto the continental shelf in the southern Weddell Sea. *Journal of Geophysical Research: Oceans*, *129*, e2023JC020700. https://doi.org/10.1029/2023JC020700

Received 10 NOV 2023
Accepted 12 OCT 2024

Author Contributions:

Supervision: J. B. Sallée
Writing – original draft: N. Steiger
Writing – review & editing: J. B. Sallée, Elin Darelius, Markus Janout, Svein Østerhus

Observed Pathways and Interannual Variability of the Warm Inflow Onto the Continental Shelf in the Southern Weddell Sea

N. Steiger[1], J. B. Sallée[1], Elin Darelius[2], Markus Janout[3], and Svein Østerhus[4]

[1]Laboratoire d'Océanographie et du Climat, Sorbonne Université, CNRS/IRD/MNHN, Paris, France, [2]Geophysical Institute, University of Bergen and Bjerknes Centre for Climate Research, Bergen, Norway, [3]Alfred-Wegener-Institute Helmholtz Center for Polar and Marine Research, Bremerhaven, Germany, [4]Norwegian Research Centre NORCE and Bjerknes Centre for Climate Research, Bergen, Norway

Abstract Model projections suggest that the continental shelf in the southern Weddell Sea may experience a shift from today's near-freezing temperature to a much warmer state, where warm water floods the shelf and basal melt rates beneath the Filchner Ronne Ice Shelf increase dramatically. Today, the Filchner Trough serves as a conduit for the southward flow of Warm Deep Water (WDW) during summer and, thus, requires continuous monitoring of its hydrographic conditions. An extensive network of moorings was installed at key sites along the inflow pathway from 2017 to 2021, to expand on existing mooring records starting in 2014. The moorings complemented with under-ice profiling floats reveal two inflow pathways, where WDW enters along the eastern flank of the Filchner Trough as well as through a smaller trough east of there. Within the observed period, 2017 and 2018 feature anomalously warm inflows. The inflow is regulated by the heaving of isopycnals over the continental slope, and the southward propagation toward Filchner Ice Shelf is two times faster during these warm years. Furthermore, the warm years coincide with low summer sea ice concentration, which enhances surface stratification through increased freshwater input and modifies sea ice-ocean stresses that both act to lift the warm water layer and increase the temperatures on the continental shelf. Finally, the recent record low sea ice conditions around the Antarctic emphasize the importance of our findings and raise concerns regarding a potentially increasing presence of WDW on the southern Weddell Sea shelf.

Plain Language Summary Melting of ice shelves, the floating extension of the Antarctic ice sheet, has been linked to the flow of relatively warm water from the deep ocean into the ocean-filled cavities underneath them. In the Weddell Sea, the shallow continental shelf is generally covered with near-freezing water, and the large Filchner Ronne Ice Shelf in the south is presently characterized by low basal melt rates. Here, we explore four to 7-year-long bottom-mounted mooring records of temperature and velocity from the region and the drift trajectories of subsurface floats. We show that the water follows two pathways onto the eastern part of the continental shelf whose relative importance varies from year to year. During years that are warmer than average, the warm water moves more rapidly across the shelf. The warm water inflow was especially large in 2017 and 2018 and appeared to be linked to anomalously low sea ice concentration. A reduced ice cover and changes in the stress at the ocean surface help to bring the warm water higher up in the water column so that it can more easily flow onto the continental shelf.

1. Introduction

The Filchner Ronne Ice Shelf (FRIS) in the southern Weddell Sea is by volume the largest of all ice shelves fringing the Antarctic ice sheet (Fox et al., 1994). It buttresses its tributary ice streams that drain about 15% of the entire ice sheet toward the ocean (Rignot et al., 2013). As of today, FRIS is considered as being relatively stable (Pritchard et al., 2012; Rignot et al., 2013) with a mass balance of -124 ± 66 Gt a^{-1} (Moholdt et al., 2014), which means that the mass gained from the upstream ice flow and precipitation is roughly balanced by calving at the ice front and melting at its base. Basal melting is determined by the transport of ocean heat into the cavity that lies beneath the ice shelf. FRIS is considered to be in a cold cavity regime (Jacobs et al., 1992), where a wide and cold continental shelf protects the ice shelf from the Warm Deep Water (WDW) that resides at mid-depth off the continental shelf. However, model projections (Hellmer et al., 2012, 2017) indicate that a shift toward a warm cavity regime is possible in the future under a high warming scenario. Warm water would then flush the continental shelf and the ice shelf cavity, leading to an up to 10 times increase in basal melt rates within less than

50 years (Thoma et al., 2015). The magnitude and timing of the projected changes in basal melt rates are disputed in different studies (Daae et al., 2020; Nissen et al., 2022; Siahaan et al., 2022) which highlights our limited understanding of the processes that drive interannual variability and long term changes.

One of the main gateways of the warm water entering the continental shelf and FRIS is provided by the Filchner Trough that intersects the shelf and connects the Filchner Ice Shelf with off-shelf waters. Inflow of warm water onto the shelf is also occurring in the Central Trough at about 44°W (Davis et al., 2022; Janout et al., 2021; Nicholls et al., 2008), but sea ice makes this trough nearly inaccessible and observations rely mainly on autonomous vehicles or tagged seals. The eastern part of the Filchner Trough and the continental slope upstream are more easily reachable by ship. In situ observations there have provided an understanding of the inflow of warm water onto the shelf and its seasonal variability. The warm water is transported into the southern Weddell Sea by the Weddell Gyre from the east and flows westward along the continental slope with the Antarctic Slope Current (ASC; Ryan et al., 2016). The prevailing easterly winds push the WDW layer downward through Ekman dynamics, creating the Antarctic Slope Front (ASF) which separates the warm ocean waters from the cold continental shelf waters. During summer, when the easterly winds weaken and surface stratification increases, the thermocline shoals and the WDW, or its modified version (mWDW), flows onto the shallow continental shelf at a depth of about 400 m (Ryan et al., 2017; Årthun et al., 2012). Once on the continental shelf, the mWDW follows the bathymetry southward along the eastern flank of the Filchner Trough toward at least 76°S (Ryan et al., 2017). The deeper Filchner Trough is filled with cold and dense Ice Shelf Water (ISW) that lies beneath the mWDW layer due to its high density. This ISW layer blocks the access of mWDW into the cavity beneath the 400–450 m thick ice shelf (Daae et al., 2020; Fretwell et al., 2013), but mWDW has been observed as far south as the ice front in 2013 (Darelius et al., 2016). While the seasonal inflow of the mWDW has been observed on the slope and on the continental shelf, there have so far been no synchronous observations across different locations to provide a broader view of the propagation of the inflow toward the Filchner Ice Shelf.

Drivers of the seasonality of the ASC and the slope front have been identified to be related to the zonal wind stress, Ekman transport, sea ice concentration, and thermohaline forcing linked to warming and cooling or sea ice production (Núñez-Riboni & Fahrbach, 2009). The seasonality of the ASC north of the Filchner Trough is linked to the seasonal cycle of the mWDW shoaling and deepening (Darelius, Fer, et al., 2024): When the current is strongest, the mWDW layer deepens; when the current is weakest, the thermocline shoals. So far, time series have been too short to analyze drivers of interannual variability of the warm water inflow onto the continental shelf in the vicinity of the Filchner Trough. The observed presence of mWDW as far south as the ice front in 2013 was hypothesized to be associated with generally weak easterly winds that lift the thermocline off the continental shelf in combination with short-lived wind events that enhance the southward transport of mWDW (Darelius et al., 2016). An exceptionally warm and prolonged inflow of warm water into the Filchner Trough in 2017 was hypothesized to result from preceded strong sea ice melt that caused increased density gradients across the ASF and increased instabilities that bring the WDW southward onto the continental shelf (Ryan et al., 2020). This warm anomaly in 2017 has also been observed within a 12-year-long temperature record below the Fimbul Ice Shelf at the Prime Meridian, 20° farther east of the Filchner Trough (Lauber et al., 2023; Lauber, Hattermann, et al., 2024), suggesting the onset of an anomalously warm period there. The observations in the Filchner Trough region have so far been too short to investigate the interannual variability in mWDW flow onto the continental shelf and its potential link to processes over the continental slope.

In this study, we make use of 4 to 7-year-long synchronous mooring records on the continental slope north of the Filchner Trough, on the Filchner Sill and on the continental shelf at 76°S to get a better understanding of the southward propagation and the variability of the warm water flow toward the Filchner Ice Shelf. We combine the mooring velocity observations with the trajectories of subsurface profiling floats to reveal pathways of the southward flow of mWDW from the continental slope onto the shelf. Then, we analyze the seasonal variability of temperature and velocity on the shelf, followed by estimates of the advection time scale of mWDW from the continental slope toward 76°S based on the mooring records and the float trajectories. We further describe the interannual variability of the mWDW presence observed over the continental slope and its propagation onto the continental shelf. We then provide insights into the drivers of the interannual variability of the warm water inflow based on sea ice and wind data as well as historical hydrographic observations and finish with a discussion.

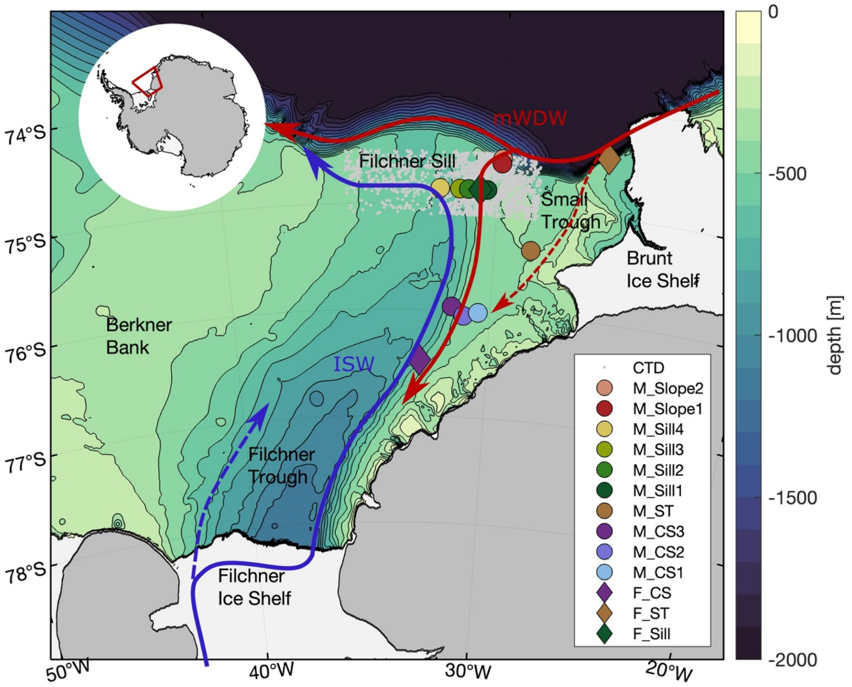

Figure 1. Overview map of the Filchner Trough region in the eastern part of the southern continental shelf in the Weddell Sea. The bathymetry is from IBCSO (Arndt et al., 2013) with marked contours every 100 m. Grounded ice is shaded dark gray and floating ice shelves are light gray. Mooring locations are marked with colored circles, historic CTD casts with gray dots, and the deployment location of the APEX floats as diamonds. Red and blue arrows are a sketch of the circulation of relevant water masses, mWDW and ISW, respectively. The inset in the upper left shows the location of the study site.

2. Data and Methods

2.1. Moorings

We use a network of oceanographic bottom-mounted moorings that were deployed during the WAPITI cruise on R/V *James Clark Ross* in February 2017 (JCR16004; Sallée, 2018). The mooring locations are shown in Figure 1 and detailed information is given in Table 1. We use a naming of the moorings according to their location with numbers from the shallowest to the deepest mooring. Two moorings were deployed on the upper part of the continental slope: M_{Slope1} and M_{Slope2} (Darelius, Janout, et al., 2023, 2024). Four moorings were deployed on the Filchner Sill: M_{Sill1}, M_{Sill2}, M_{Sill3}, and M_{Sill4} (Steiger & Sallée, 2023), plus one mooring at the entrance to the "Small Trough" on the eastern continental shelf: M_{ST} (Steiger & Sallée, 2023). We use additional three moorings M_{CS1}, M_{CS2}, and M_{CS3} on the continental shelf over the eastern flank of the Filchner Trough at about 76°S (Janout et al., 2022). These three moorings are operated since 2014 (Schröder et al., 2017a, 2017b, 2017c) and were redeployed during the RV Polarstern expedition PS111 in February 2018 (Schröder, 2018; Schröder et al., 2019a, 2019b, 2019c). All moorings were recovered during the RV Polarstern-expedition PS124 in February 2021 (Hellmer & Holtappels, 2021). The moorings were equipped with current meters (ADCPs from RDI and/or Aanderaa RCMs) and hydrographic sensors (SBE37, SBE39 and SBE56 from Seabird Electronics). We present the hydrographic data as conservative temperature Θ and absolute salinity SA using the TEOS-10 equation of state (McDougall & Barker, 2011). Since many of the moorings only had one salinity sensor attached, we assume a constant salinity for the calculation of conservative temperature, which induces an error of about 0.001°C. We define ISW as water with a conservative temperature of $\Theta < -1.9$°C and mWDW as water with $\Theta > -1.7$°C. All data are hourly averages, and we filter the temperature and velocity time series with a 2nd order low-pass Butterworth filter with a cutoff frequency of 66 hr to remove tides. The velocity data are additionally smoothed with a 30-day running mean. Further treatment of the data, if applied, is described in the text. In order to produce a continuous long-term temperature record at M_{CS1} that was redeployed with slightly different bottom and sensor depths, we linearly interpolate the data onto a constant grid with 20 m vertical resolution.

Table 1
Details of Moorings and Floats Used in This Study

Name	Orig. Name	Latitude/ longitude	Start/ end	Depth [m]	Depth of hydrogaphy sensors [m]	Depth of velocity measurements [m]
M_{Sill4}	S2E17	74°51.04'S/ 32°05.41'W	23.02.2017 01.03.2021	600	590, 567, 542, 517, 492, 467, 442, 417, 392, 367, 342, 317	586:2:498[a]
M_{Sill3}	P2	74°51.04'S/ 31°22.72'W	12.02.2017 16.02.2021	580	569*,[a], 550, 520, 495, 470, 445, 420, 395, 370	570[a], 480[a]
M_{Sill2}	P1	74°51.03'S/ 31°03.72'W	12.02.2017 16.02.2021	548	540*,[a], 515, 490, 465, 448, 423, 398, 373, 348	534:4:454[a] 424:16:56[a]
M_{Sill1}	P4	74°51.00'S/ 30°23.01'W	11.02.2017 15.02.2021	435	428*,[a], 403, 379, 335, 313, 303	430:4:366[a], 313[a]
M_{ST}	P5	75°23.38'S/ 28°38.22'W	09.02.2017 09.03.2021	437	430*,[a], 407, 382, 362, 333, 323	431[a], 384[a], 335[a]
M_{Slope2}	M3[b]	74°33.00'S/ 29°54.48'W	24.02.2017 14.02.2021	740	716, 707*, 682, 657, 632, 604*, 579, 554, 529*, 503:25:353, 328*, 303	484:16:52
M_{Slope1}	M6[b]	74°35.70S/ 29°54.97'W	24.02.2017 13.02.2021	530	505, 496*, 471, 456, 431*, 404, 379, 354*, 328	310:8:38
M_{CS1}	A252-1[c]	76°05.49'S/ 30°28.24'W	05.01.2014 21.01.2016	450	430*, 332*	
	A252-2[d]	76°05.47'S/ 30°28.19'W	22.01.2016 04.02.2018	455	412*, 397*, 372*, 348*, 334*	
	A252-3	76°05.54'S/ 30°28.14'W	05.02.2018 01.03.2021	467	443*, 428, 403, 378, 350*	449, 349
M_{CS2}	A253-3	76°02.74'S/ 31°01.42'W	05.02.2018 01.03.2021	471	443*, 423, 403, 383, 354*	453, 353
M_{CS3}	A254-3	75°57.68'S/ 31°29.79'W	05.02.2018 02.03.2021	606	578*, 553, 528, 481, 461, 441, 405*	400
F_{ST}	P12682[e]	74°27.16'S/ 26°10.99'W	10.02.2017 07.01.2021	400	–	–
F_{Sill}	P12703[e]	74°51.17'S/ 30°38.78'W	12.02.2017 30.10.2020	400	–	–
F_{CS}	P12684[e]	76°28.38'S/ 32°43.08'W	18.02.2017 14.01.2021	250	–	–

Note. The depth of hydrography sensors refers to temperature; * marks the depths with additional conductivity measurements. The depths of velocity measurements are only given if used. The depth for the floats refers to their parking depth. [a]Sensor run out of battery before recovery. [b]Darelius, Fer, et al. (2024) (their M_{740} and M_{530}). [c]Ryan et al. (2017) (their $M_{30.5W}$). [d]Ryan et al. (2020) (their $M_{30.5W}$). [e]Sallée et al. (2024).

2.2. Floats

During the WAPITI cruise in February 2017, Apex profiling floats were deployed at locations close to the mooring sites. The floats carried a SeaBird SBE41 hydrography sensor, and they were positioned beneath sea ice with the RAFOS system (Rossby et al., 1986) every six hours based on timed arrivals of signals from sound sources attached to three of the moorings. More information on the floats and the position assignment is provided in Sallée et al. (2024). We here use three of these floats, F_{ST}, F_{Sill}, and F_{CS}, that were deployed in the Small Trough, on the Filchner Sill, and farther south on the continental shelf, respectively (Table 1). The first two floats were parked to drift at 400 m depth, the depth at which mWDW is typically found in the Filchner Sill region. This depth agrees with the mean maximum temperature depth based on historic CTD profiles within the area of 20–45°W and 73–76°S. F_{CS} was parked to drift at 250 m depth to avoid it entering the ice shelf cavity.

2.3. CTD

We complement CTD-data from the deployment and recovery cruises (Sallée, 2018; Tippenhauer et al., 2023) with available historical CTD data collected during summer (DJF) both by ship and instrumented Weddell Seals over the Filchner Sill (28°30’W to 35°30’W, 74’S to 75°06’S, Figure 1) from 1979 and on. All profiles are linearly interpolated onto a vertical 1 m grid. The number of profiles within the area of interest varies strongly between the years (Figure 8b), and to give equal weight to each year, we calculate yearly mean profiles of temperature and salinity.

2.4. Forcing Data

We use daily averaged sea ice concentration and zonal 10 m winds on a $0.25° \times 0.25°$ grid from ERA5 reanalysis (Hersbach et al., 2018) and daily sea ice velocity data from the National Snow and Ice Data Center (NSIDC) (Tschudi et al., 2019) with a 25 km × 25 km spatial resolution. We focus the surface forcing on a region over the continental slope (slope region; similar to Ryan et al., 2020) bounded by 35°W to 15°W and 750–3,500 m depth.

The sea ice drift data are linearly interpolated onto the ERA5 grid and used to calculate ocean surface stress τ as a weighted contribution of ice-water and air-water stresses (Dotto et al., 2018; Martin et al., 2016):

$$\vec{\tau} = \alpha\,\vec{\tau}_{iw} + (1-\alpha)\,\vec{\tau}_{aw}, \tag{1}$$

where α is the sea ice concentration, $\tau_{iw} = \rho_w c_{iw} |\vec{u}_i| \vec{u}_i$ is the ice-water stress, and $\tau_{aw} = \rho_a c_d |\vec{u}_a| \vec{u}_a$ is the air-water stress, with the water and air densities of $\rho_w = 1025$ kg m^{-3}, $\rho_a = 1.25$ kg m^{-3}, respectively, and the air-water and ice-water drag coefficients of $c_{iw} = 5.5 \times 10^{-3}$ and $c_d = 1.25 \times 10^{-3}$, respectively. We note that the ocean velocities within the ASC (at M_{Slope1}) are in the order of magnitude of 0.1 m s^{-1} during summer (Darelius, Fer, et al., 2024), that is, two orders of magnitude smaller than the wind speed, but of similar magnitude as the sea ice drift. Unfortunately, we are not aware of available spatial fields of ocean currents that could be included in the net surface stress calculation. Geostrophic currents from satellite altimetry data (Auger et al., 2022) are of poor quality for the calculation of the curl and are missing over the slope in our study area.

Based on the ocean surface stress, we calculate the ocean stress curl as

$$\text{curl} = (\mathbf{k} \times \nabla) \cdot \vec{\tau}. \tag{2}$$

Assuming a constant Coriolis forcing within our study region ($f = -1.4 \times 10^{-4}$ s^{-1}), ocean stress curl is proportional to Ekman pumping with a factor of $\left(f\rho_a\right)^{-1}$. Positive values correspond to downwelling and negative values correspond to upwelling. Coastal convergence is not taken into account, because sea ice drift data are not available along the coast (see missing data along the coast in Figures 7i–7l).

2.5. Calculation of Heat Content, Temperature Transport, Advection Times and Correlation

We calculate the heat content at the moorings as the depth-integral of the difference between the conservative temperature and the lowest temperature found in the data, $\Theta_0 = -2.24$°C, according to:

$$H = \int_{z_2}^{z_1} \rho_w c_p (\Theta - \Theta_0)\, dz, \tag{3}$$

where $\rho_w = 1{,}027.85$ kg m^{-3} is the density, $c_p = 3{,}991.9$ J (kg K)$^{-1}$ is the specific heat capacity, and z_2 and z_1 are the depths of the lower and the upper temperature sensors. Where intermediate temperature sensors failed, a linear interpolation is used; where upper- or lowermost sensors failed, the missing data are filled with the data from the nearest sensor. Note that the moorings only provide temperature records within the lower part of the water column and the captured thickness varies between the moorings; the heat content is consequently underestimated, especially during peak periods of mWDW inflow when the mWDW layer extends beyond the upper temperature sensor, and the magnitude of the heat content is not comparable between the moorings. We are here mainly interested in the time variability, and we use the heat content time series for lag-correlations and advection times between the moorings. We alternatively tested our analysis based on the temperature time series at one depth level; the results are similar to when using the heat content time series, but are sensitive to the chosen depth level.

In addition to the heat content, we calculate the meridional temperature transport Q at each of the moorings as:

$$Q = \int_{z_2}^{z_1} \rho_w c_p v(\Theta - \Theta_0)\, dz. \tag{4}$$

The meridional velocity v presented is linearly interpolated onto the depth-levels of the temperature sensors. We present the seasonal cycle of the temperature transport together with the seasonal cycle of temperature and velocity. Because the velocity sensors ran out of battery at different times after 2 years or more, we include two full yearly cycles (starting at the deployment time) for each of the presented moorings. To calculate the southward heat transport on the continental shelf and toward the ice shelf, we would need the knowledge of the width of the current, which the moorings do not provide. The temperature transport can be used as a proxy of the seasonal variability of the southward heat transport.

The lag-correlation of the unfiltered heat content at different moorings is calculated using the normalized correlation coefficient based on Sciremammano (1979). In addition to the correlation lag (Lag), we determine the advection times "Δt" of the mWDW between the moorings as the time difference between the maxima of the heat content time series, both for the climatology (mean Δt) and for the individual years (2017–2020). To determine the timing of the seasonal maxima, we smooth the time series with a 30-day running mean which minimizes the impact of short term events such as storms and waves. To calculate advection velocity, we estimate the distance between the mooring locations as a straight line for M_{Sill1}/M_{ST} to M_{CS1}. Between M_{Slope1} and M_{Sill1} we use the distance along the 450 m isobaths. While there is no direct connection between M_{Slope1} and M_{ST}, we assume that the variability along the continental slope north of the Small Trough is comparable to the variability at M_{Slope1}. We calculate the advection time between M_{Slope1} (representative for the slope north of the Small Trough) and M_{ST} based on the mooring records, but we calculate the distance as a straight line between M_{ST} and the closest 450 m isobaths on the slope north of it.

To analyze the interannual variability of the temperature measured by the moorings and to set it in context with the forcing data, we use anomalies of the time series, for which we subtract the climatological seasonal cycle from the full time series. The seasonal cycle is based on the available time range for the moorings and the period from 2012 to 2021 for the forcing data, unless otherwise stated.

We examine the interannual variability of isotherm depth by linearly interpolating the temperature records onto a vertical grid of 5 m resolution. Note that in the study area, isotherms are mostly parallel to isopycnals, and changes in the thermocline correspond to changes in the pycnocline.

3. Results

3.1. Mean Pathways of mWDW and ISW on the Eastern Continental Shelf

Previous studies within the Filchner Trough area (e.g., Årthun et al., 2012; Darelius, Makinson, et al., 2014; Janout et al., 2021; Ryan et al., 2017) have been based on single mooring locations or snapshots from ship- or seal-based CTD measurements to gain insight into the water masses on the continental shelf and their circulation pathways. Here we make use of simultaneous measurements at various locations to investigate the circulation of mWDW and ISW in the Filchner Trough region based on oceanographic moorings and profiling floats. Over the continental slope, the time-averaged velocities from the moorings (M_{Slope2} and M_{Slope1}; Figure 2a) show a strong westward flow of mWDW (more than 0.15 m s^{-1} at its maximum), which is part of the persistent ASC (more about its vertical structure and the seasonal variability in Darelius, Fer, et al., 2024). On the continental shelf, the mWDW follows isobaths southward ($v < 0$) along the eastern flank of the Filchner Sill (M_{Sill1} and M_{Sill2}) and east of it through the Small Trough (M_{ST}) (Figures 2e–2g). At these shallow moorings, the presence of ISW is low or non-existent (Figures 2j–2l). Farther west, over the deeper part within the Filchner Trough (M_{Sill3}, M_{Sill4} and M_{CS3}), velocities within the thick bottom layer of ISW (Figures A1c–A1d), are northward ($v > 0$) and up to

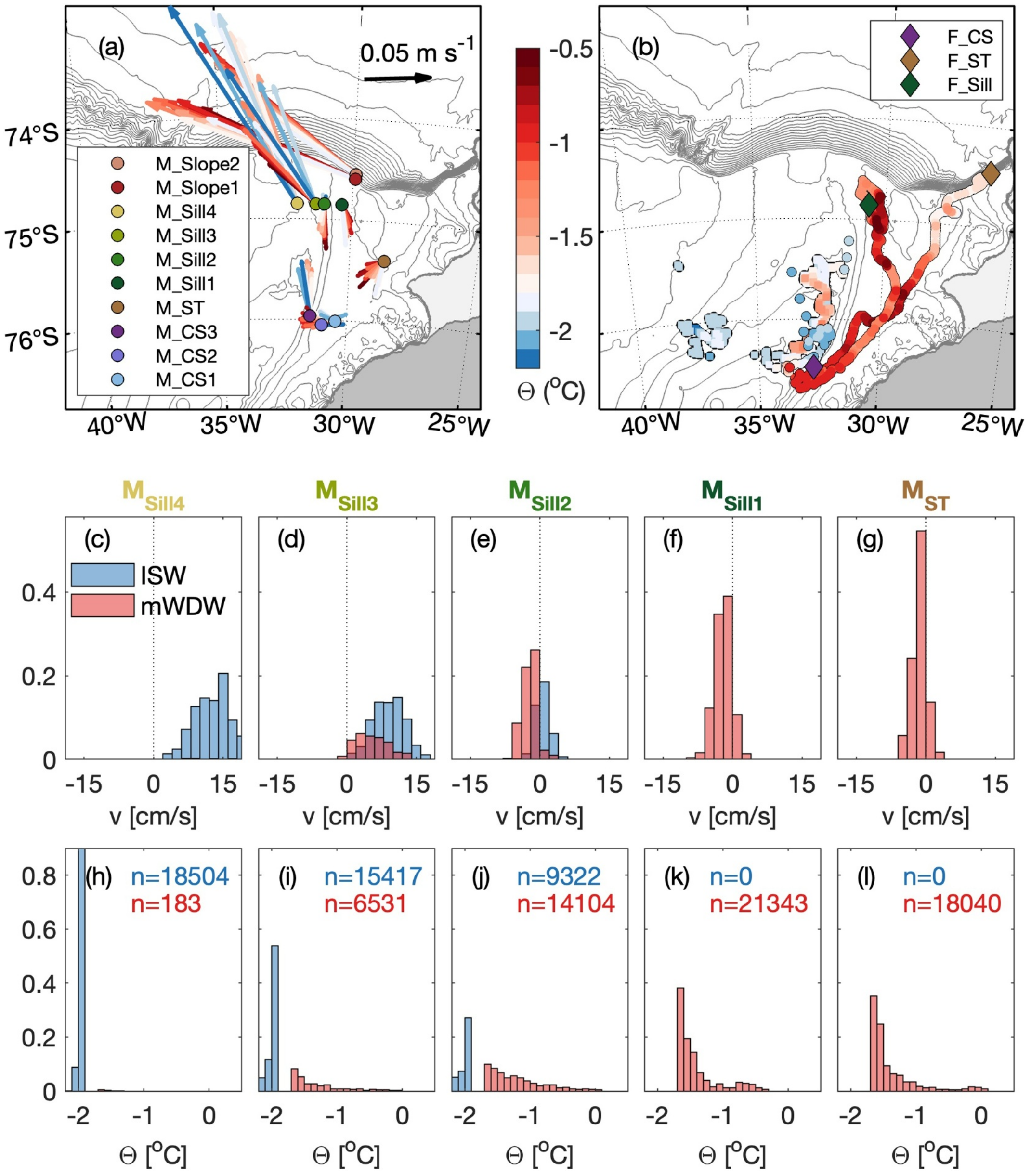

Figure 2. (a) Velocities from the moorings averaged within 0.1°C temperature bins. Arrows symbolize the mean direction and speed (see black reference vector in the upper right corner) within each temperature bin (color-coded according to the colorbar). The full velocity records are included for each mooring, but note that the covered time period vary between moorings (see Table 1 and Figure 3f). (b) Temperature (according to colorbar) along the float trajectories of F_{ST} (brown diamond, through the Small Trough), F_{Sill} (green diamond, along the eastern flank), and F_{CS} (purple diamond, within the Filchner Trough) at their parking depths of 400, 400, and 250 m, respectively. The diamonds mark their deployment locations. The contours in the background in (a, b) correspond to bathymetry as in Figures 1c–1g Histograms of the meridional velocity (v) for the temperature bins within the temperature ranges of ISW (<-1.9°C, blue) and mWDW (between -1.7°C and -0.8°C, red) for each mooring over the sill and Small Trough from west to east. (h–l) Histograms as in (c–g) of the temperature bins within the temperature ranges of ISW and mWDW. The histograms in (c–l) are normalized by the total number of data points within both water masses, where the number of data points for ISW (blue) and mWDW (red) is indicated for each mooring in the corresponding panel. In (a, c–l) we only include velocity data at the two depth sensors closest to 10 and 100 m above bottom. Temperature is linearly interpolated onto these depths.

0.15 m s^{-1}. This northward flow of waters below the surface freezing point indicates an outflow of ISW (Foldvik et al., 2004). At M_{Sill2}, where coexisting ISW and mWDW layers are measured, the velocities are southward in the mWDW layer and weakly northward in the ISW layer (Figures 2a and 2e).

The mWDW is thus entering the continental shelf over shallower isobaths of the flank of the Filchner Trough and east of it, and not through the deeper parts of the trough which is filled with northward flowing (dense) ISW. The southward flow along the eastern flank of the Filchner Trough as seen from the moorings M_{Sill2} and M_{Sill1} is also well captured by the float F_{Sill} that was deployed in February 2017 on the eastern flank of the Filchner Sill close to mooring M_{Sill1} (Figure 2b, green diamond). The float first drifted northward toward the continental slope, then turned southward to pass again mooring M_{Sill1} and M_{CS1}, reaching as far south as 76°30'S. The temperatures along the float's trajectory at 400 m depth lie between −1.5°C and −0.5°C, thus, within the range of mWDW. While this southward flow along the eastern flank of the Filchner Trough has been recorded over several years (Ryan et al., 2017), mooring M_{ST} and float F_{ST} confirm, in addition, a southward flow of mWDW through the Small Trough at about 27°W (Figures 2a and 2b), previously captured by ship-based transects or seals (Nicholls et al., 2009; Årthun et al., 2012). F_{ST} also measured temperatures within the range of mWDW (between −1.7°C and −0.8°C) at its drift depth of 400 m. For comparison, a third float F_{CS} that was deployed farther south remained within the deeper Filchner Trough, capturing mainly ISW despite its shallow drift depth of 250 m. While this float recirculated within the Filchner Trough without leaving it, the ISW captured by the moorings over the sill is associated with strong northward velocities, indicating the ISW overflow leaving the Filchner Trough. CTD-sections across the eastern flank in summer 2013 suggest maximum northward flow of ISW at about 500 m depth (Darelius, Makinson, et al., 2014, their Figure 5). The drift depth of the float might consequently have been too shallow, its location too far west of the eastern flank for the float to be advected northward out of the Filchner Trough with the strong ISW current, or it got caught in a long-lived eddy.

3.2. Seasonal Variability of the mWDW Inflow

We will now focus on a subset of the moorings (M_{Slope1}, M_{Sill1}, M_{ST}, M_{CS1}) to describe the temperature variability of the mWDW inflow and its propagation from the continental slope onto the shelf. The mWDW is located below a layer of colder Winter Water (WW) at all locations (Figures 3a–3d). We here use moorings over shallow depths (<500 m) where mWDW is at the bottom. Deeper inside the Filchner Trough, cold and dense ISW is present beneath the mWDW throughout the whole year (Figures A1b–A1d). ISW appears occasionally at mooring M_{CS1} (in early 2019 and 2020, Figure 3d). The seasonal shift between ISW and mWDW at this location has been described by Ryan et al. (2017), and we here focus solely on the mWDW inflow.

Over the continental slope (M_{Slope1}, Figure 3a), the mWDW is present at the bottom throughout most of the year. The temperatures show a strong seasonal cycle with warmest waters of up to 0°C in late February. There is also a seasonal cycle in the depth of the −1.7°C-isotherm; the mWDW layer reaches up to about 370 m during austral summer and is pushed down toward the bottom (530 m) during austral winter. The seasonal cycle in the hydrography above the upper part of the slope is tightly connected to the (observed) seasonal variability of the ASC at this location (Darelius, Fer, et al., 2024) and has been suggested to be driven by seasonal changes in the winds (Årthun et al., 2012) and/or upper ocean hydrography (Hattermann, 2018). The concurrent mooring records show the propagation of the seasonal signal at the continental slope onto the shelf via the Filchner Sill and through the Small Trough toward at least 76°S. The moorings located on the continental shelf (M_{Sill1}, M_{ST}, M_{CS1}, Figures 3b–3d) capture a seasonal mWDW signal during summer; in winter the layer of mWDW at the continental slope is too deep to reach onto the shelf, where WW occupies the whole water column all the way down to the bottom (Figures 3a–3d). The seasonal signal of mWDW reaches the mooring at 76°S (M_{CS1}, Figure 3d) every year in early April, albeit with variable temperature and duration.

While the seasonal presence of mWDW often is referred to as a seasonal inflow, it is not clear whether the actual inflow, that is, the current, is seasonal or whether it is a quasi-constant inflow that advects a seasonal signal in temperature. The meridional velocities at the moorings M_{Sill1} and M_{ST} do show a seasonal signal with a weak southward and occasionally reversed flow at the beginning of austral summer (November to February) followed by stronger southward velocities from March onward (Figures 3f, 4a, 4b, 4d, and 4e). The southward velocities on the Filchner Sill (M_{Sill1}) and in the Small Trough (M_{ST}) start increasing rapidly while the temperatures reach their maximum, which shows an offset similar to the continental slope where temperatures decrease while the slope current peaks (Figure 3f and Darelius, Fer, et al., 2024). The mWDW thus already appears on the continental shelf while the southward velocities at the mooring sites are still weak. Once the temperatures reach their maximum, southward velocities have strengthened, resulting in a maximum southward temperature transport in March (Figures 4g and 4h). Occasionally, for example, during the strong temperature peak in the Small Trough in the

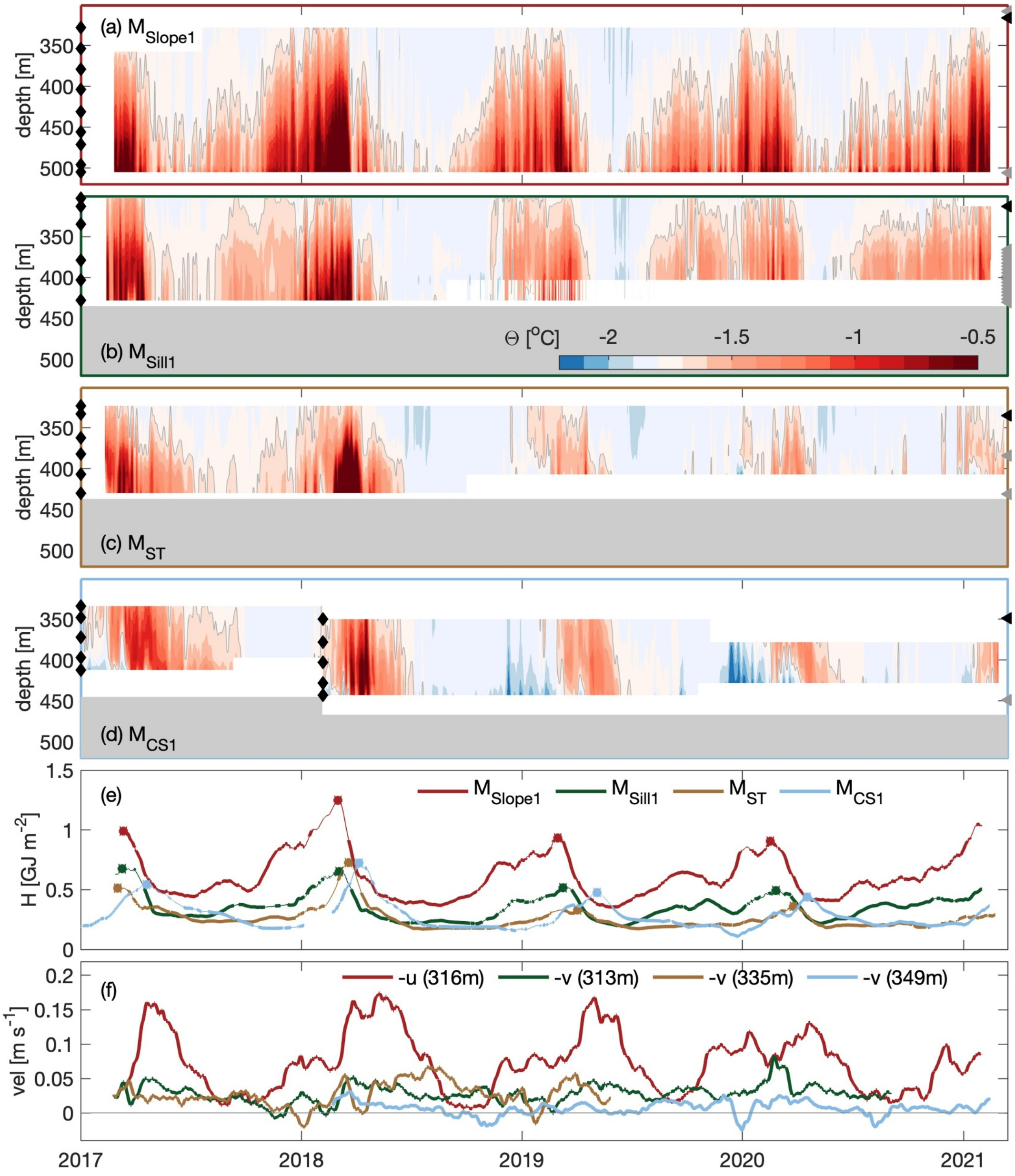

Figure 3. Temperature time series from 2017 to 2021 at the shallowest moorings along the inflow pathway. (a–d) Hovmoller diagrams of the temperature records from moorings (a) M_{Slope1}, (b) M_{Sill1}, (c) M_{ST}, and (d) M_{CS1}. The gray contour marks the threshold for the mWDW (−1.7°C). Gray shading indicates the bottom. The black diamonds on the left *y*-axis show the depth of the temperature sensors, and the gray triangles on the right *y*-axis show the depths of the velocity measurements, with the depths used in (f) highlighted in black. Mooring M_{CS1} was redeployed in January 2018 at a slightly different water depth and with different depths of the temperature sensors. (e) Heat content (H) time series of the moorings, smoothed with a 30-day running mean. Stars mark the seasonal peaks in heat content. Periods where the −1.7°C-isobath is above the uppermost sensor are plotted with thin lines. (f) Velocity time series of the moorings smoothed with a 30-day running window. We show westward velocities (-u) for M_{Slope1} and southward velocities (-v) for the other moorings at the depths given in brackets.

beginning of 2018, the temperature peak follows strong southward velocities, indicating a strengthened southward transport of mWDW. Farther south at 76°S (M_{CS1}), the velocities and thus the temperature transport are generally small (Figures 4c, 4f, and 4i), but increased southward velocities precede the warmer temperatures, suggesting that the mWDW is transported here by the southward currents.

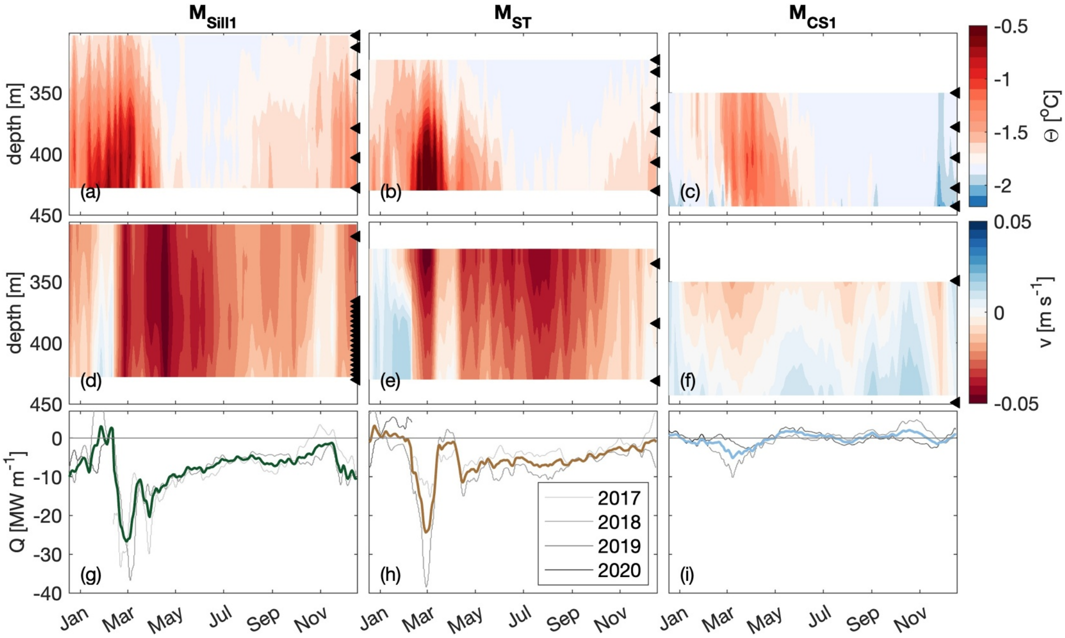

Figure 4. Seasonal cycle of conservative temperature Θ (a–c) and meridional velocity v (d–f) at the moorings M_{Sill1}, M_{ST}, and M_{CS1}. The meridional velocity is linearly interpolated onto the depth-levels of the temperature sensors and smoothed with a 30-day running mean. The black triangles on the right y-axis show the depths of the measurements. (g–i) Shows the seasonal cycle of the meridional temperature transport Q (Equation 4) in color and for each year in gray according to the legend in (h).

3.3. Southward Advection of mWDW

Using the records from the moorings and the floats, we quantify the advection timescale of the mWDW flow from the continental slope onto the shelf. We use the correlation lag (Lag) of the unfiltered heat content time series from the moorings, and, alternatively, the time difference of the heat content peaks in summer between the moorings (Δt) to solely focus on the mWDW inflow (Table 2). Note that there are uncertainties in the determination of the timing of the maximum peak in the heat content given that not the whole water column is captured and due to the high short-term variability of the heat content which we try to overcome by smoothing the time series. While Δt only captures the advection of the seasonal heat content peak during summer, the Lag also incorporates the impact of a seasonally changing current speed—and even reversed current direction (Figures 3f and Ryan et al., 2017)—, as well as the onset of the winter convection and short-term variability. We present a time range for the advection

Table 2
Distance (Dist), Lag-Correlation (Corr, Lag), Advection Times (Δt) and Velocities (Vel) Between the Four Moorings M_{Slope1}, M_{Sill1}, M_{ST}, and M_{CS1}

	Moorings					Floats			Estimate
	Dist (km)	Corr	Lag (days)	Δt (days), mean (2017, 18, 19, 20)	Vel (cm s^{-1}), mean (2017, 18, 19, 20)	Dist (km)	Δt (days)	Vel (cm s^{-1})	Δt (weeks)
M_{Slope1}–M_{Sill1}	47	0.65	9	9 (**8**, ***1***, 9, 9)	6 (**6**, ***27***, 6, 6)	-	-	-	1
M_{Slope1}–M_{ST}	78	0.53	19	18 (***11***, **16**, 32, 38)	5 (***45***, **5**, 3, 2)	-	-	-	2–5
M_{Sill1}–M_{CS}	135	0.60	56	38 (**25**, **32**, 57, 52)	4 (**7**, **5**, 3, 3)	167	40	5	4–8
M_{ST}–M_{CS}	90	0.80	26	29 (**22**, **17**, 34, 23)	4 (**3**, **6**, 3, 5)	92	12	9	2–5
M_{Slope1}–M_{CS}	182	*0.47*	*56*	46 (**33**, **33**, 66, 61)	4 (**6**, **6**, 3, 3)	-	-	-	5–9

Note. The correlations are based on the full (unfiltered) heat content time series and the advection times on the seasonal peaks of the smoothed heat content (Figure 3e, see Section 2). The correlations are significant on a 95% significance level, except the correlation between M_{Slope1} and M_{CS1} (in italic), which is significant on a 90% significance level. The advection times and velocities are given for the climatology (mean) and for the individual years (2017–2020, where the "warm years" 2017 and 2018 are in bold and unrealistic values in italic). For comparison, we present the distance, Lagrangian advection time and velocity between M_{Sill1}–M_{CS1} and M_{ST}–M_{CS1} based on the float trajectories, where we use the times when F_{Sill} and F_{ST} pass closest to the corresponding mooring locations. The last column shows a concluding estimated maximum range for the advection times, based on the different methods and the year-to-year variation.

between the different mooring sites, based on the two different calculations and year-to-year variations (last column in Table 2). The time for the signal to reach from M_{Slope1} to M_{Sill1} is about 1 week, and from M_{Slope1} to M_{ST} about 2–5 weeks (Table 2). From then on, the temperature signal propagates for about 4–8 weeks from M_{Sill1} to M_{CS1} and about 2–5 weeks from M_{ST} to M_{CS1}. In total, the signal takes about 5–9 weeks from the continental slope (M_{Slope1}) to 76°S (M_{CS1}) via the two pathways.

Comparing the advection time Δt of the maximum peak year by year (Table 2) shows that there is a strong interannual variability and that, in general, the heat content peak traveled about twice as fast in 2017 and 2018 (~0.05–0.06 m s^{-1}) compared to 2019 and 2020 (~0.03 m s^{-1}). Unfortunately, none of the velocity measurements on the continental shelf cover the whole 4-year period to compare the interannual variability in the advection of the warm water peak with the velocities measured at the moorings. The velocity measurements at M_{CS1} cover the period from 2018 to 2020 and confirm a stronger southward current in 2018 (0.03 m s^{-1}) compared to 2019 (0.01 m s^{-1}) and 2020 (0.02 m s^{-1}) (Figure 3f), where we used an average in depth (449 and 349 m depth) and the time period between the heat content peak at M_{Sill1} and M_{CS1}. While mean currents at M_{CS1} are indeed stronger during the warm inflow years, this is not the case at M_{Sill1} and at M_{ST} (Figure 3). We note, however, that the seasonal warm inflow is not aligned with the strongest southward velocities at these locations (Figure 4).

The floats F_{Sill} and F_{ST} deployed in 2017 reveal additional information on the Lagrangian pathway of the mWDW southward toward the ice shelf (Figure 2b) and they provide another estimate of the advection timescale between the moorings, as they passed close to the mooring locations. Float F_{ST} took a direct path through the Small Trough from M_{ST} to M_{CS1} (along-path distance between the moorings of 92 km compared to a straight line distance of 90 km) in only 12 days (compared to 22 days advection time inferred from the heat content peak) (Table 2). The float passed between the two moorings during a period of strong currents, with an average speed of ~0.1 m s^{-1} based on the drift speed of F_{ST} and the southward velocity at M_{ST}. The other float F_{Sill} that started over the Filchner Sill took a less direct trajectory between M_{Sill1} and M_{CS1} (167 km compared to 135 km) and moved slower between the two moorings (40 days) compared to the advection time based on the heat content peak (25 days). We conclude that the floats provide relevant information on the possible pathway and temperature between the two moorings, but advection times cannot be inferred from float trajectories solely and require the use of long-term observing systems such as moorings.

Both the moorings and the floats suggest two pathways of the mWDW into the Filchner Trough: over the Filchner Sill and farther east through the Small Trough (Figures 2a and 2b). Since the moorings M_{Sill1} and M_{ST} were deployed at similar isobaths, we assume them to be directly comparable as they are typically occupied by the same density water. The measurements show a generally lower heat content at M_{ST} and less presence of mWDW during summer (Figures 3b, 3c, and 3e). However, in 2018, the temperatures in the Small Trough reached up to 0°C (Figure 3d), which is warmer than the temperatures recorded at the other moorings. While the heat content time series farther south at M_{CS1} (Figure 3e) typically follows the heat content time series at M_{Sill1}, the pronounced temperature peak in 2018 resembles instead the peak at M_{ST}. The records suggest that, in some years, the mWDW turns onto the continental shelf at the opening to the Small Trough, but in other years, it continues along the continental slope and flows into the Filchner Trough over the Filchner Sill.

3.4. Interannual Variability of the mWDW Inflow

The temperature records at all moorings along the mWDW inflow pathways (Figure 3) show a similar seasonal cycle and interannual variability. It is apparent in the time series on the continental shelf (M_{Sill1}, M_{ST}, and M_{CS1}), that the presence of mWDW in 2017 is longer there compared to the other years (Ryan et al., 2020), even persisting throughout the wintertime over the Filchner Sill and within the Small Trough (M_{Sill1} and M_{ST}). All moorings also show that the inflow in summer 2018 is the warmest within the 4-year measurement period. We thus identify the years 2017 and 2018 as "warm inflow years." With the 4-year long time series, we can now investigate the propagation of the interannual temperature variability from the slope onto the shelf. The seasonal cycle in temperature is directly linked to heaving of the isotherms over the continental slope (Darelius, Fer, et al., 2024), but it is not clear whether interannual temperature variability is caused by anomalies in the interface heaving, or whether it is caused by variability in the water masses present above the continental slope north of the shelf.

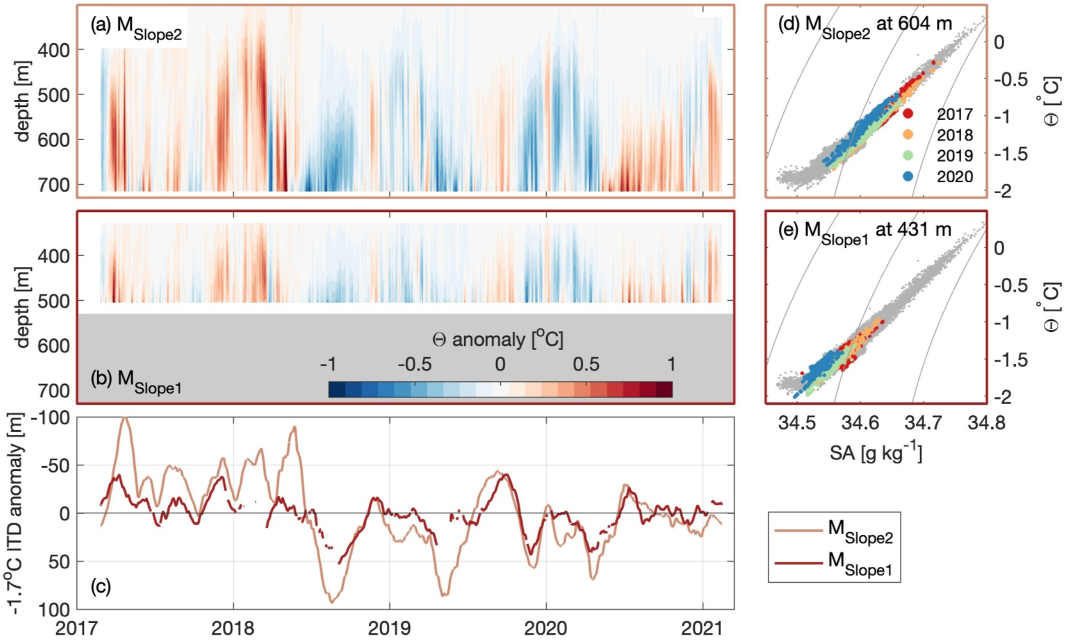

Figure 5. Hovmoller-diagram of the temperature anomaly (from the seasonal cycle) at (a) M_{Slope2} and (b) M_{Slope1}. (c) Time series of the −1.7°C isotherm depth (ITD) anomaly at M_{Slope2} and M_{Slope1}, smoothed with a 30-day running mean. The ITD is calculated through linear interpolation onto a vertical grid of 5 m resolution. (d) TS-diagram of de-seasoned daily averages at 604 m depth at M_{Slope2} and (e) TS-diagram of de-seasoned daily averages at 431 m depth at M_{Slope1}. The different years in (d, e) are color coded according to the legend in (d). The gray dots in (d, e) are from all sensors at M_{Slope1} and M_{Slope2} and the gray contours are isolines of density.

The temperature anomalies at the moorings M_{Slope1} and M_{Slope2} over the continental slope show indeed higher temperatures during the years 2017 and 2018, followed by generally colder temperatures during 2019 and 2020 (Figures 5a and 5b). This interannual change from a warm toward a cold period is also seen in the isotherm depth anomaly (Figure 5c), which shows a shoaling of the isotherm within the mWDW temperature range during 2017 and the first half of 2018, followed by several periods of deepened isotherms. The interannual changes in isotherm depth are visible at both moorings over the continental slope, but more so for M_{Slope2} compared to M_{Slope1}. The movement of the isotherm suggests that the interannual variability is caused by a heaving of the water masses over the slope rather than a change in the water masses themselves. This is further supported by the interannual changes within the temperature-salinity space (Figures 5d and 5e), where the warmer temperatures in 2017 and 2018 are associated with a movement along the mixing line between WDW and WW rather than a shift only in temperature.

As shown previously, the temperature signal propagates from the continental slope onto the shelf. The interannual variability is consistent between the moorings (Figures 6a–6h). The extended temperature record at 76°S (M_{CS1}, Figures 6g and 6h), covering the period 2014–2021, further shows that the summer temperatures in 2017 and 2018 were exceptionally high within this 7-year period. The mooring over the continental slope (M_{Slope1}) shows that the mWDW was not being pushed down toward the bottom by the overlying WW during winter 2017, unlike the other winter seasons (Figure 3a). The mWDW layer persisted throughout 2017 over the sill, and 2017 was followed by even higher temperatures at the beginning of 2018. The warm inflow was then shut off abruptly in June 2018 associated with a strong deepening of the isotherms over the slope (Figure 5c) and a strong increase in the slope current velocities observed at M_{Slope1} (Figure 3f). None of the moorings measured mWDW at the bottom during the second half of 2018. The temperatures in the following years were slightly below the average again at all moorings (Figures 6b, 6d, 6f, and 6h), although peak temperatures about the upper part of the slope increased in November 2019 (Darelius, Dundas, et al., 2023). At the time of the mooring recovery in early February 2021, the temperatures at M_{Slope1} suggest that the 2021 inflow might be warmer than average (Figures 6a and 6b), but an extended time series is needed to confirm this.

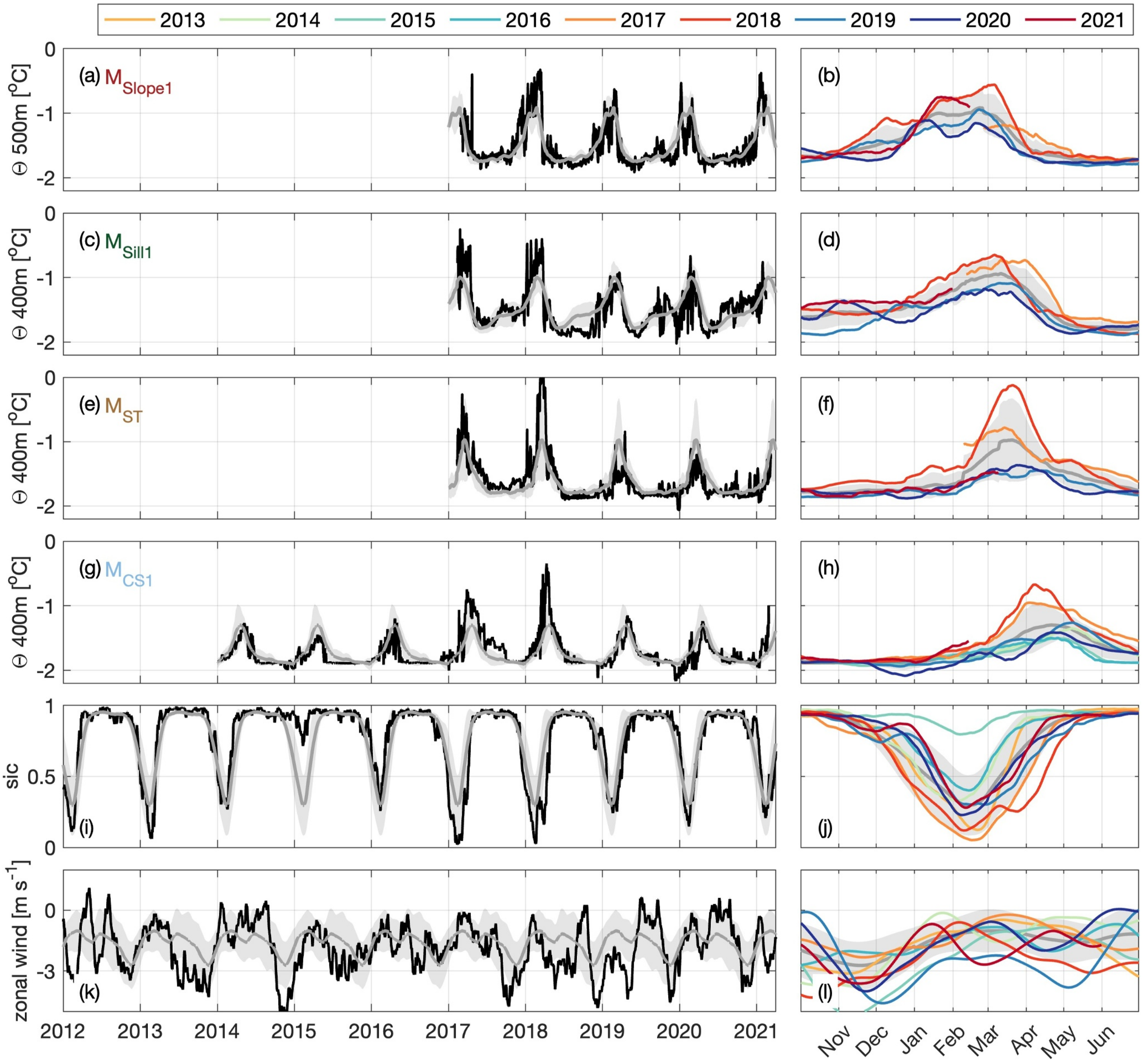

Figure 6. Time series and climatology of observed bottom temperature, sea ice concentration (SIC) and zonal wind. Temperature is shown from mooring M_{Slope1} at 503 m depth (a, b), mooring M_{Sill1} at 403 m (c, d), mooring M_{ST} at 407 m (e, f), and M_{CS1} at 404 m (g, h). SIC (i, j) and zonal 10 m wind (k, l) are averaged over the slope region, see Figure 7. The left panels show the daily averaged time series (black) together with the climatology (gray) and its standard deviation (gray shading). The climatology is smoothed with a 30-day moving window. The right panels show the seasonal cycle of the climatology (gray) with its standard deviation (gray shading) and the seasonal cycle for each year (smoothed with a 30-day running mean), color-coded according to the legend. Orange-red colors correspond to "warm inflow years" (2013, 2017, 2018, 2021), and green-blue colors correspond to "cold inflow years" (2014–2016, 2019–2020). For clarity, the wind time series is smoothed with a 60-day moving window instead (k, l) and first filtered with a 30-day lowpass filter in (l). The climatology is averaged over the existing time periods for the moorings and over the period of 2012–2021 for SIC and zonal wind.

3.5. Drivers of the Interannual Variability

We now investigate potential drivers of the observed interannual variability in temperatures observed at all moorings along the mWDW inflow pathway. The seasonal variability has previously been linked to the seasonal changes in surface stratification (Hattermann, 2018) and the seasonality in the prevailing easterly winds (Årthun et al., 2012). Increased stratification in summer through the presence of a shallow upper pycnocline below the fresh Surface Water would allow the lower pycnocline (and, thus, the thermocline) separating WW from

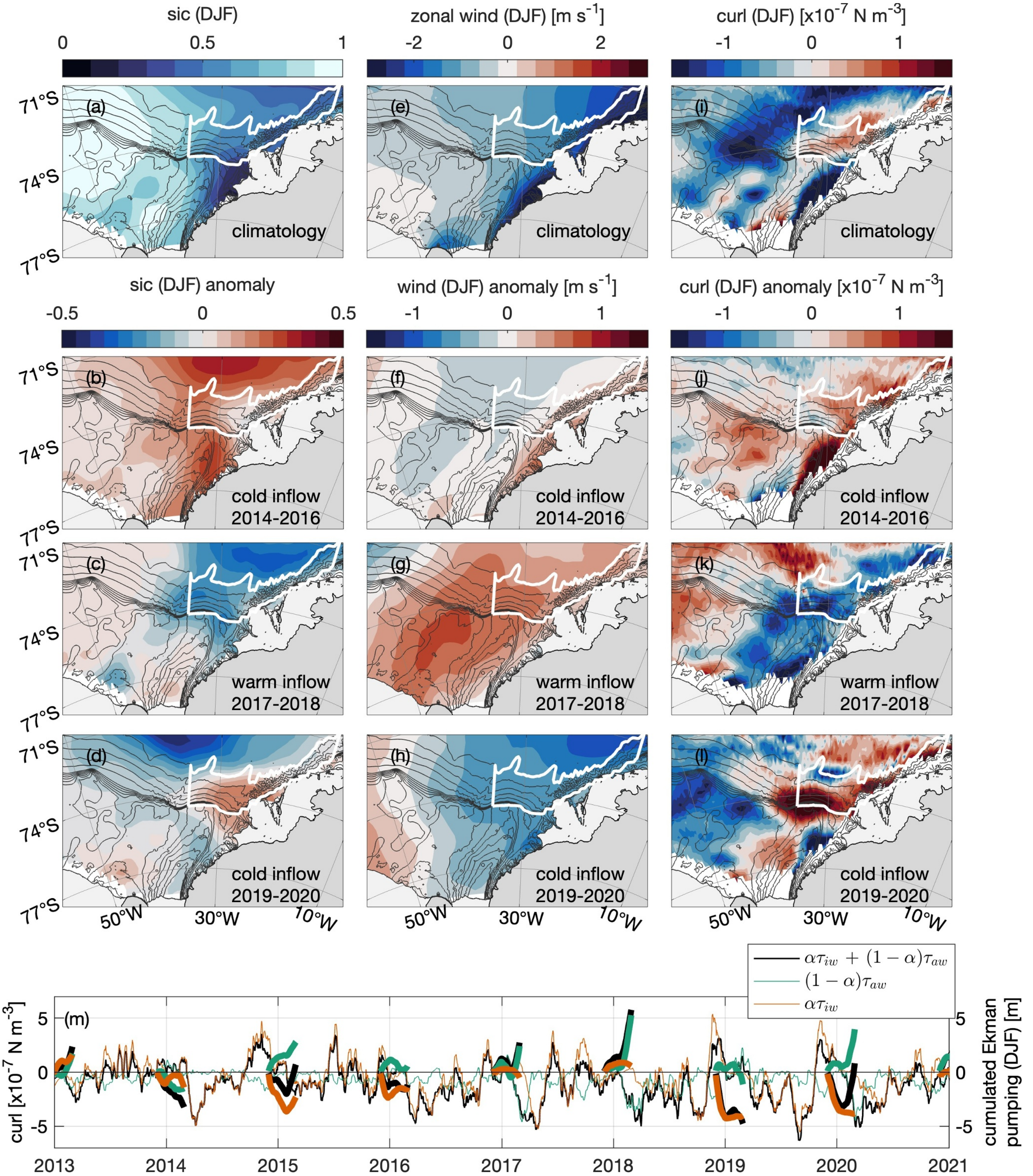

Figure 7. Spatial map of southern Weddell Sea with summer (DJF) climatology and anomalies for sea ice concentration (SIC; a–d), zonal wind (e–h), and ocean surface stress curl (i–l). The upper panels (a, e, i) show the summer climatologies for the period of 2012–2021. The anomalies are seasonal anomalies from the climatology averaged over the years within the different periods: cold inflow period in 2014–2016 (b, f, j), warm inflow period in 2017–2018 (c, g, k) and cold inflow period 2019–2020 (d, h, l). The contours show the bathymetry as in Figure 1. The light gray area is ice shelf, the dark gray area is grounded ice and the white contour is the slope region used for time-series of the forcing. (m) shows the time series of the absolute curl (with a 30-day running mean applied) as thin lines, left y-axis and the time-integrated absolute Ekman pumping from December to February each year as thick lines, right y-axis. The curl and cumulated Ekman pumping are derived from the total ocean surface stress (black), as well as the wind stress over ice-free areas ($(1-\alpha)\tau_{aw}$, green) and the sea ice stress over ice-covered areas ($\alpha\tau_{iw}$, red).

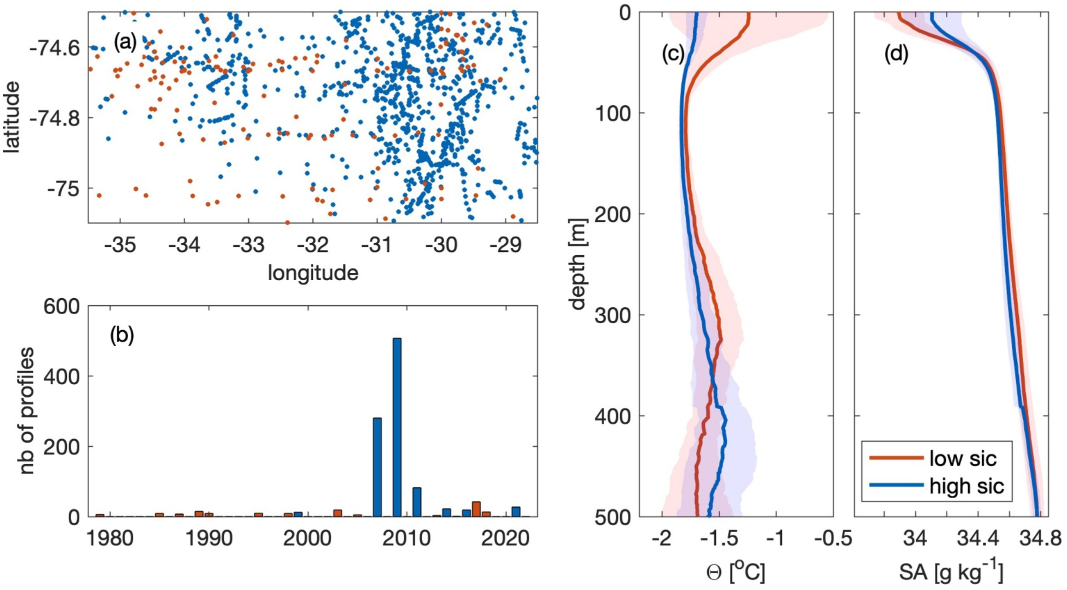

Figure 8. Historic CTD profiles over the Filchner Sill for years with low SIC (red) and years with high summer SIC (blue) in summer (DJF) relative to the climatology. (a) Location of the profiles over the Filchner Sill (see also Figure 1). (b) Number of profiles for the different years. Composites for (c) temperature and (d) salinity profiles for low SIC years (red) and high SIC years (blue) with the standard deviation in shading. The composites are calculated from yearly averaged profiles to give equal weight to each year.

(m)WDW to relax (as Ekman pumping would primarily affect the upper pycnocline); mWDW would hence be found at shallower depths above the continental slope (Hattermann, 2018). Easterly winds create a southward Ekman transport that deepens the isopycnal along the continental slope (Sverdrup, 1953) and impedes the flow of mWDW onto the continental shelf. Previous studies have suggested that a weakening of the easterlies during summer allows for a seasonal inflow of mWDW onto the continental shelf (Årthun et al., 2012) and that, for example, the warm inflow in 2013 would be associated with weaker easterly winds (Darelius et al., 2016).

We here analyze the interannual variability of zonal wind and sea ice concentration over the continental slope, as well as their combined effect on the ocean surface stress curl, that is, Ekman pumping. We divide the 7 years of observations into three periods: The "cold inflow period" in 2014–2016, the "warm inflow period" in 2017–2018, and the "cold inflow period" in 2019–2020 based on the FMA mean at M_{CS1} (Figure B1a). Since we are interested in the contribution of the forcing on the seasonal mWDW inflow, we focus on the summer average of the forcing, using the 3 months preceding the warm water peak over the continental slope M_{Slope1}, that is, December to February (DJF) each year.

The winds over the Filchner Trough area are generally easterly and vary on all timescales. The 10 m zonal winds above the Filchner Sill show a seasonal cycle in the climatology with weakening winds over the summer period (Figure 6k), in agreement with Årthun et al. (2012). However, there is no clear link between the interannual variability in the 7 years-long time period at M_{CS1} and the local 10 m zonal wind (Figures 6h and 6l) and we find neither significant correlation between the local 10 m wind and the temperature record at M_{CS1}, nor between their de-seasoned time series. While the summers of 2014 and 2015 are preceded by maintained strong easterlies over the Filchner Trough area (above 3 m s^{-1}), the winds remain close to the climatology between mid-2015 and mid-2017, followed again by anomalously strong easterlies before summer seasons, although less persistent than previously. To assess their contribution to the seasonal inflow of mWDW, we focus on the DJF-averages of the zonal winds. They do show generally weaker easterlies during 2017 and 2018 and slightly stronger easterlies in the two following years (Figures B1c, 7g, and 7h). This signal is in agreement with the interannual variability observed at the moorings and possibly influence the access of mWDW onto the continental shelf. However, the positive anomalies in 2017 and 2018 are weak (Figure B1c) and the weaker easterlies along the coast during 2014–2016 should induce a warm inflow, which is in contrast to the observations from the moorings.

Sea ice typically covers the entire Filchner Trough area during winter, but the sea ice cover opens up from the east during summer (Figure 7a), with a minimum sea ice concentration occurring in February (Figures 6i and 6j).

February is also when the temperature peaks over the continental slope at M_{Slope1}, 2 months before the temperature peaks at M_{CS1} (Table 2). The interannual variability in sea ice concentration is strikingly similar to the temperatures at the moorings: The two warm inflow years in 2017 and 2018 are associated with anomalously low sea ice concentration that drops far below the 10-year average, while the preceding 3 years (2014–2016) and the following 2 years (2019–2020) are characterized by average or higher sea ice concentration (Figures B1b, 6i, and 6j). The sea ice concentration in the area was also anomalously low in 2013 when mWDW was observed to reach the Filchner Ice Shelf front possibly linked to an exceptionally warm inflow (Darelius et al., 2016).

The shift from a period with average/high summer sea ice concentration (2014–2016) to low sea ice concentration (2017–2018) is not only visible locally; it can be seen over the entire Weddell Sea (Figures 7b and 7c), and it coincides with the observed Southern Ocean-wide decline in sea ice extent starting in 2016 (Eayrs et al., 2021). Following the two warm inflow years, the sea ice concentration was again rather high during 2019 and 2020 locally over the Filchner Sill and toward the east along the coast but anomalously low over the rest of the Weddell Sea (Figure 7d).

Sea ice may influence the thermocline depth and the warm water inflow through different mechanisms. On one side, sea ice impacts the ocean surface stress through the difference in ice-ocean stress compared to the air-ocean stress (e.g., Martin et al., 2016). On the other side, sea ice formation and melting influence the upper ocean stratification as it creates a seasonal, shallow pycnocline during summer and erodes it during winter (Hattermann, 2018). Ryan et al. (2020) suggested that a strong surface stratification in early 2017 led to a stronger slope front and, thus, eddy shedding that, in turn, flattened the slope front, leading to increased transport of mWDW onto the continental shelf.

To explore the impact of sea ice on the upper ocean stratification and the upper pycnocline, the mooring measurements do unfortunately not reach high enough up in the water column. However, historic CTD measurements over the Filchner Sill starting in 1989 provide more information on the stratification in the upper water column on a (somewhat) longer timescale. Based on the sea ice concentration averaged over a box within 20–35°W and 73–75.5°S, we extract the years with low sea ice concentration during summer (DJF) versus the years with high sea ice concentration relative to the multi-annual mean (1989–2021) (Figure B1). Composites of the available CTD profiles over the Filchner Sill for these two cases show that the years with low sea ice concentration have a fresh and warm surface layer and that it is associated with a shallower mWDW layer (320 m depth instead of 450 m depth) that can access the continental shelf more easily (Figure 8).

To analyze the combined impact of sea ice and winds on the mWDW inflow onto the continental shelf through the ocean surface stress and thus Ekman dynamics, we calculate the ocean surface stress curl (Equations 1 and 2). While the time series of the local surface stress curl within the region over the continental slope upstream of the Filchner Trough has a variability on various time scales (Figure 7m), we are here interested in the drivers of the seasonal variability of mWDW inflow. The DJF-anomalies of the ocean surface stress curl (Figures 7j, 7k, and 7l) show anomalous upwelling (negative anomaly) over the eastern part of the continental shelf and eastward along the coast during 2017 and 2018, and anomalous downwelling (positive anomaly) during the years before and after. The local time-integrated absolute Ekman pumping over DJF each year (thick black lines in Figure 7m), within the slope region indeed shows upwelling in 2017–2018, and the high temperatures in 2017 and 2018 might thus be supported by upwelling over the slope. Note that the integrated Ekman pumping calculated here reveals an upwelling of only up to 5 m, which is an order of magnitude smaller than the vertical movement of the isotherms measured by the moorings over the continental slope (Figure 5). However, we here only calculate the local impact of the surface stress curl away from the coast (we do not account for coastal convergence, as the stress data do not extend toward the coast), but the seasonal heaving is observed all along the slope south of the Weddell gyre (Hattermann, 2018; Lauber, de Steur, et al., 2024) and possibly produced upstream of the Filchner Trough region. Since ocean surface stress depends on winds, sea ice concentration and sea ice drift (Equation 1), both the winds and the sea ice can cause this interannual variability in the surface stress curl. Hence, we calculate the curl of the sea ice weighted air-ocean stress ($(1-\alpha)\tau_{aw}$) and the sea ice weighted ice-ocean stress ($\alpha\tau_{iw}$) separately (Figure 7m). It shows that the total ocean surface stress curl is driven by the contribution from ice-ocean stress, that is, sea ice drift, during most of the year, but the contribution to the Ekman pumping during summer varies from year to year, possibly depending on the timing of sea ice retreat. Specifically in the warm inflow years 2017 and 2018 in which there was little sea ice and weaker easterly winds, upwelling is almost entirely controlled by the air-ocean stress. We note that the integration and mean over DJF are sensitive to the chosen time period and the chosen region. However, the reduced sea ice concentration in summer 2017 and 2018 and the Ekman-driven upwelling are consistent over the slope in front of the Filchner Trough and upstream of it for the period preceding the warm water inflow.

4. Discussion and Conclusions

We used a network of concurrent moorings and profiling floats on the Weddell Sea continental shelf to improve our understanding of the mWDW pathways from the continental slope onto the shelf and southward toward the Filchner Ice Shelf. The warm water flows across the continental slope in late summer or early fall, and is transported southward along topographically controlled pathways toward the ice shelf. Earlier studies showed that the eastern flank of the Filchner Trough is the major mWDW pathway on the southeastern continental shelf, and in addition our new observations highlight a second prominent pathway along the Small Trough, located in the shallower region east of the Filchner Trough. Our data suggest that the relative importance of either pathway changes interannually, and that the observed warm inflow in 2018 was dominated from the Small Trough-inflow. However, the moorings only provide spatially restricted measurements and these variations might originate from a shift of the mWDW core on the Filchner Sill and within the Small Trough. The drivers of such internannual variability remain unclear, and could be a profitable subject of future modeling experiments. Regardless of the mWDW pathways, the timescale to reach from the continental slope toward 76°S—nearly half way toward the Filchner Ice Shelf front—, is about 5–9 weeks. These timescales vary interannually with nearly twice as fast currents during the warmer years of 2017 and 2018.

While the temperature records on the Filchner Sill and in the Small Trough (M_{Sill1}/M_{ST}) show a seasonal cycle with warmest temperatures in January to March, the meridional velocities are weak and even northward during January and early February (Figures 3f and 4). The southward velocities are instead strongest from March to June at M_{Sill1} and from March to November at M_{ST}, when the temperatures are lowest. This coincides approximately with the period of maximum ASC along the upper part of the continental slope (Darelius, Fer, et al., 2024). This raises the question of where the mWDW observed at the mooring locations during the first part of the summer season enters the continental shelf. The floats suggest a southward flow through the Small Trough and along the eastern flank of the Filchner Trough in February 2017, and the mooring M_{CS1} farther south at 76°S also indicates a southward flow before the arrival of mWDW. During the end of February and March, the velocities are indeed southward during the period when peak temperatures are observed at M_{Sill1} and M_{ST}, which contributes to a sharp peak in the temperature transport. However, mWDW already present at the shallow moorings on the continental shelf before this warm inflow is not associated with southward velocities there and must have entered the continental shelf elsewhere. For example, the mWDW already present at M_{Sill1} after October 2017 seems to have its core farther west at M_{Sill2} at about 500 m depth (Figure A1b), where velocities are indeed southward (not shown here).

The two warm inflow years of 2017 and 2018 are here set into context within the 2014–2021 period recorded by the mooring M_{CS1} at 76°S. While 7 years may not allow to quantitatively link the summertime mWDW inflow with the driving mechanisms, our records nevertheless indicate a clear connection between sea ice concentration and mWDW inflow (Figures 6 and B1). Previous studies that only had shorter time periods at hand (Darelius et al., 2016; Årthun et al., 2012) focused on the weakening of easterly winds as a driver for the seasonal inflow of mWDW and the anomalously far reach of mWDW toward the ice shelf in 2013. Based on our recent observations, we suggest that sea ice concentration might instead be a leading driver of the interannual variability of the inflow, or at least be important for modulating the impact of winds on the mWDW inflow. While the easterly winds are weaker during 2017 and 2018, the reduced sea ice concentration is a more prominent feature. Historic CTD observations over the Filchner Sill show that anomalously low summer sea ice concentration is associated with increased surface stratification and a shoaling of the mWDW layer over the continental slope as suggested by Ryan et al. (2020) for the 2017 inflow. In addition, early sea ice retreat over the continental slope during summer influences the ocean surface stress through more mobile sea ice and larger exposure of the ocean surface to the atmosphere, favoring anomalous Ekman upwelling (Figure 7k). The local Ekman upwelling is small but we argue that it is possibly enhanced by upwelling along the coast upstream of the Filchner Trough to produce the strong vertical movement of isotherms seen over the continental slope (Figure 5c) that promote the accessibility of mWDW onto the continental shelf as seen in 2017 and 2018. Whether the shoaling of mWDW is primarily caused by the increased surface stratification following the mechanism explained in Hattermann (2018) or by the changes in the surface stress curl is challenging to disentangle given the observations at hand. Multi-year measurements of temperature and salinity over the whole water column would help to determine changes in surface stratification and to quantify variations in water masses along potential density surfaces. However, both mechanisms—the shoaling of mWDW and increased surface stratification—promote enhanced mWDW transport onto the continental shelf in 2017 and 2018. Note that the calculation of the ocean stress curl is prone to uncertainties due to used parameterizations, a low resolution of the surface data, and the exclusion of ocean currents. The ocean surface stress assuming a stagnant ocean is generally more negative in our study area than if we include geostrophic currents from satellite altimetry data (Auger et al., 2022, and their extended version from AVISO, https://doi.org/10.24400/527896/a01-2022.010), but the monthly stress anomalies from the seasonal cycle remain similar within our study area.

Another mechanism that may drive increased mWDW inflow during years of low sea ice is through reduced Dense Shelf Water (DSW) outflow. Low sea ice during summer can furthermore be the consequence of low sea ice production in the region during the preceding winter and a consequent reduced HSSW or DSW production. A modeling study by Morrison et al. (2020) suggests that the flow of warm water onto the Antarctic continental shelf is driven by the export of DSW from the shelf, such that reduced DSW production would lead to reduced mWDW inflow. The underlying mechanism is a lowered sea surface height during pulses of dense water leaving the shelf, which causes a net onshore transport of warm water. Darelius, Daae, et al. (2023) showed that this mechanism is at play in the area west of the Filchner Trough, where dense DSW is steered downslope by a ridge cross-cutting the continental slope (Darelius & Wåhlin, 2007), and that it causes a reduction in the thermocline depth of about 200 m and higher temperatures on the shelf west of the trough than east of it. Teske et al. (2024) suggested, based on a model study, that the mechanism is important also within the Filchner Trough, and that a seasonally varying outflow is causing the seasonal inflow. There is, however, no observed seasonality in the DSW outflow velocity (Darelius, Strand, et al., 2014), and the seasonality in the model is likely linked to the fact that the model used in Teske et al. (2024) lacks an ice shelf cavity, which means that the modeled dense water is HSSW instead of ISW, and therefore more seasonal than it should be as the ISW looses seasonal signal by the long residence time in the FRIS cavity. We note that both the dense outflow (Daae et al., 2018) and the warm inflow (Darelius et al., 2016) have occasionally been observed to be correlated with the along-coast wind suggesting that a link between outflow and inflow does exist. We are currently not able to quantify neither the warm inflow nor the dense outflow, so a potential connection on interannual time-scales and the link with sea ice production is unfortunately beyond the scope of this study.

The anomalously high temperatures on the shelf in 2017 and 2018 coincide with the onset of a "warm period" beneath the Fimbul Ice Shelf (Lauber et al., 2023) about 20° farther east from the Filchner Trough, suggesting a link to larger scale processes. The warming at Fimbul follows a colder period (2013–2016) and lasts at least until the end of the published records in 2021 (Lauber, Hattermann, et al., 2024). While the seasonal variability in thermocline height above the slope north of the Fimbul Ice Shelf is similar to that observed at mooring M_{Slope1}/M_{Slope2} (Lauber, de Steur, et al., 2024), there is only a very weak seasonality in the temperatures within the cavity and the arrival of warm water is highly episodic and linked to cyclonic eddies (Lauber, Hattermann, et al., 2024). It is consequently not obvious that interannual variability at the two sites is driven by similar mechanisms, although the simultaneous onset of the "warm periods" at the two locations is striking. We note that the season 2016–2017 was characterized by widespread anomalies in the Southern Ocean atmosphere, ocean, and sea ice states, possibly associated with a large El Niño event that year (Eayrs et al., 2021; Stuecker et al., 2017).

While the warm water inflow was substantially larger in 2017 and 2018 compared to the other years within the observational period, it is unclear whether the mWDW reached the ice front in these warm inflow years. Existing CTD observations along the ice front taken in February 2018 do not show a mWDW-signal (Janout et al., 2021), but the mWDW would not reach the ice shelf before April or May considering the time it takes to cross the continental shelf (Table 2; Darelius et al., 2016). The southward continuation of the warm inflow depends on several factors such as the blocking effect of the ISW layer inside the Filchner Trough (Daae et al., 2020) and the strength of the southward current that transports the warm water toward the ice shelf (Darelius et al., 2016). The 2013-propagation of mWDW all the way toward the ice front was explained by generally weak easterly winds that allow the thermocline over the continental slope to relax, interrupted by strong short-term storms that enhance the southward transport of the mWDW along the eastern flank of the Filchner Trough once it has crossed the continental slope. For the 2017 and 2018 mWDW inflows, we do not observe this clear pattern in the local winds and instead suggest the sea ice as the main driver for the upwelling of mWDW over the continental slope. Interestingly, the local sea ice concentration was also anomalously low in 2013 (Figures 6i and Darelius et al., 2016), suggesting that these two drivers may have acted together to bring mWDW toward the ice front. In 2017 and 2018, basal melt rates at 40 km inside the cavity of the Filchner Ice Shelf were estimated with ApRES measurements to be about 1–2 m yr^{-1} (Hattermann et al., 2021; Vaňková & Nicholls, 2022) and smaller in 2018 compared to 2017. Hattermann et al. (2021) did not link this reduction in melt rates to mWDW inflow, but to a shift in the HSSW origin during 2018 from Berkner mode water close to the surface freezing point to Ronne mode water that is as cold as −2.25°C (Figures A1b–A1d). So far, mWDW has only been observed to enter the FRIS cavity west of Berkner Island, on the Ronne side of the ice shelf (Davis et al., 2022). However, due to the lack of observations, we cannot exclude an impact of mWDW inflow on basal melting in the northeastern part of the Filchner Ice Shelf, where the mWDW may enter the cavity, at different locations or closer to the ice front than the existing ApRES measurements. While satellite-derived melt rates show generally stronger melting at the northeastern part of the Filchner Ice Shelf (Adusumilli et al., 2020; Moholdt et al., 2014) the data is not sufficient to support a potential role of mWDW on basal melt rates.

Appendix A: Temperature Time Series Over the Sill

(See Figure A1).

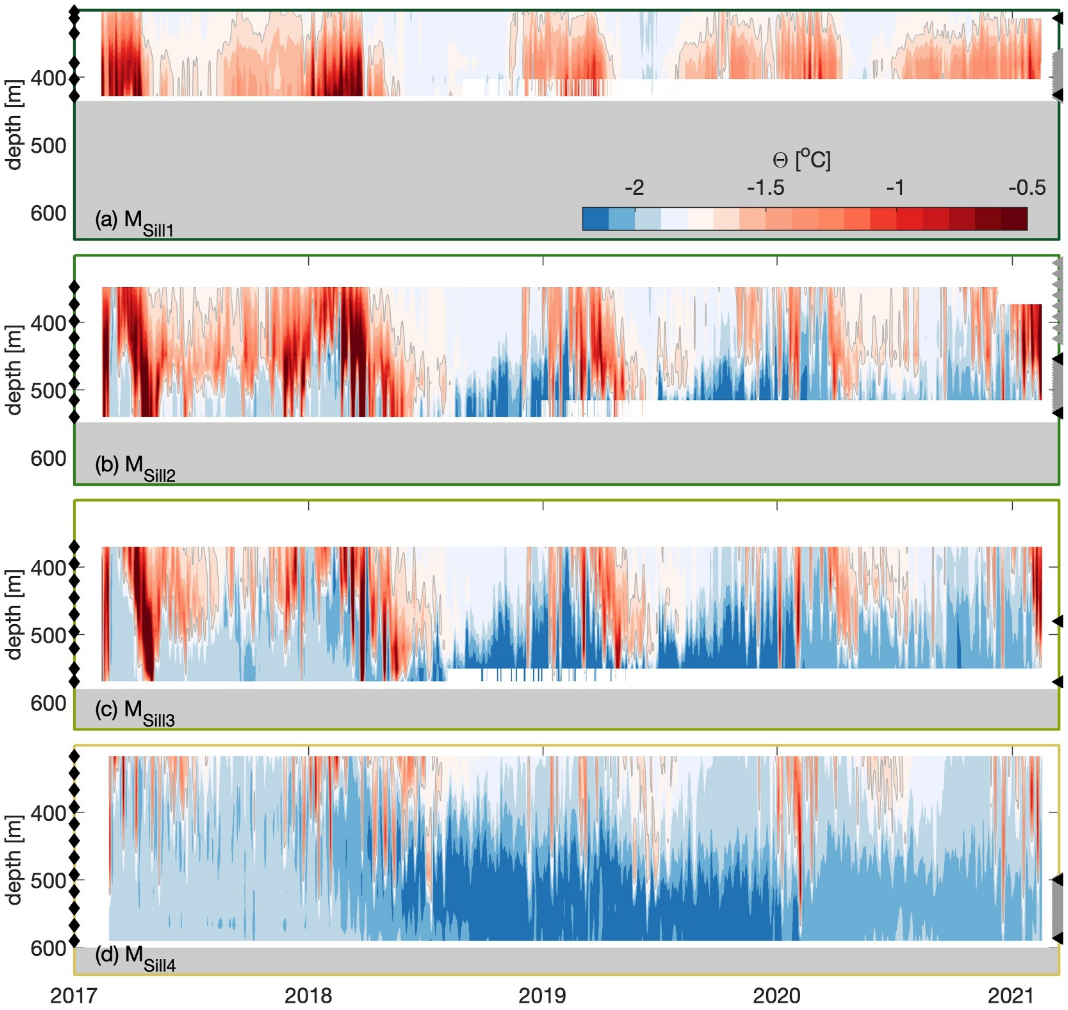

Figure A1. Hovmoller diagrams of the temperature records from moorings (a) M_{Sill1}, (b) M_{Sill2}, (c) M_{Sill3}, and (d) M_{Sill4}. The gray contour marks the threshold for the mWDW (−1.7°C). Gray shading indicates the bottom. The black diamonds on the left *y*-axis show the depths of the temperature sensors, and the gray triangles on the right *y*-axis show the depths of the velocity measurements, with the depths used in Figure 2 highlighted in black.

Appendix B: Anomaly Time Series of Temperature and Forcing Over the Filchner Sill

(See Figure B1).

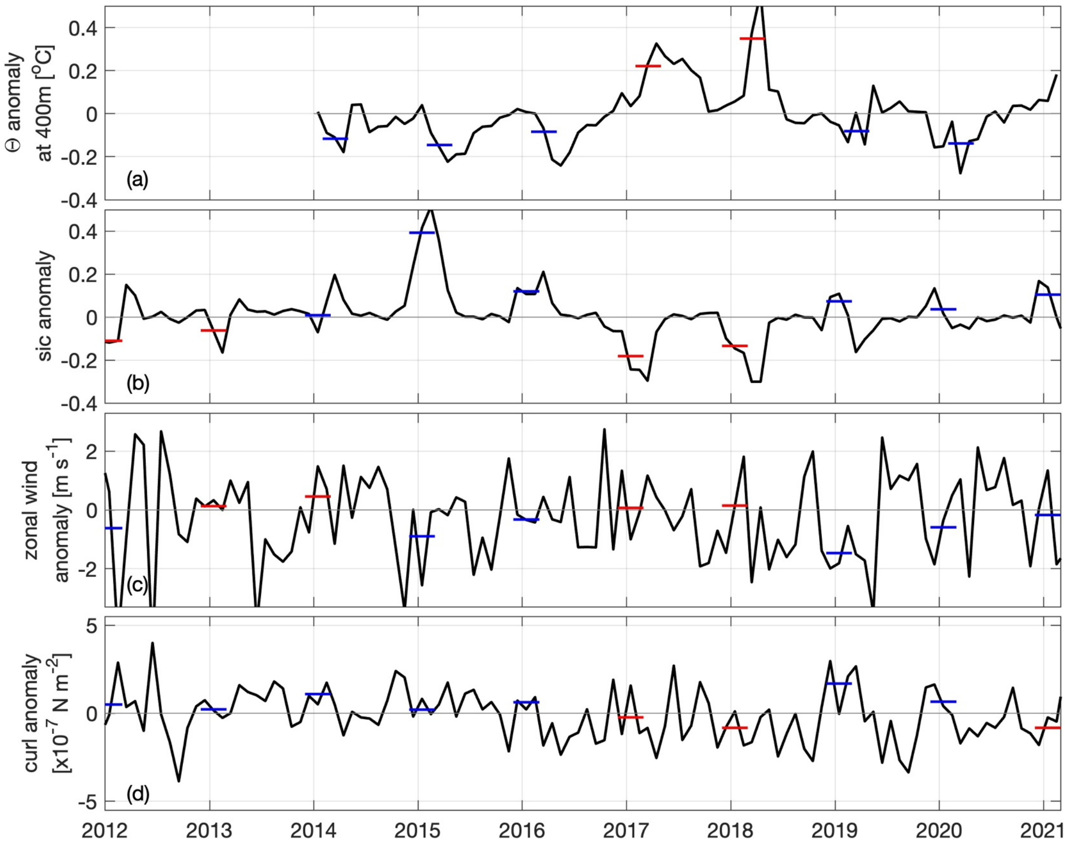

Figure B1. Monthly averaged anomaly time series of (a) 400 m temperature at M_{CS1}, (b) sea ice concentration (SIC), (b) 10 m zonal winds and (c) ocean stress curl over the slope of the continental shelf (see white region in Figure 7). The red and blue horizontal bars show the summer mean (FMA for the temperature at M_{CS1} in a and DJF for the forcing in b–d) where the color coding symbolizes whether the summer mean would support a warm inflow of mWDW (red) or suppress it (blue).

Data Availability Statement

Records from the oceanographic moorings are available as:

- M_{Slope2} https://doi.org/10.1594/PANGAEA.962043 (M3, Darelius, Janout, et al., 2023),
- M_{Slope1} https://doi.org/10.1594/PANGAEA.964715 (M6, Darelius, Janout, et al., 2024).
- M_{CS1}, M_{CS2}, M_{CS3} https://doi.org/10.1594/PANGAEA.944430 (A252-3, A253-3, A254-3, Janout et al., 2022); https://doi.org/10.1594/PANGAEA.903104, https://doi.org/10.1594/PANGAEA.903315, https://doi.org/10.1594/PANGAEA.903317, (A252-2, A253-2, A254-2, Schröder et al., 2019a; Schröder et al., 2019b, 2019c), https://doi.org/10.1594/PANGAEA.875931, https://doi.org/10.1594/PANGAEA.875932, https://doi.org/10.1594/PANGAEA.875933, (A252-1, A253-1, A254-1, Schröder et al., 2017a; Schröder et al., 2017b, 2017c).
- M_{ST}, M_{Sill1}, M_{Sill2} and M_{Sill3} https://doi.org/10.17882/100680 (P5, P4, P1, P2, Steiger & Sallée, 2023)

Seal data included in this study are available for 2007, 2009, 2011 and 2017 and downloaded from MEOP (www.meop.net) (Treasure et al., 2017). Historical ship data are available for the individual years as:

- 1979. https://doi.org/10.1594/PANGAEA.527410, (Østerhus, 2006c),
- 1985. https://doi.org/10.1594/PANGAEA.527497, (Østerhus, 2006a),
- 1987. https://doi.org/10.1594/PANGAEA.734988, (Østerhus, 2010),

- 1989. https://doi.org/10.1594/PANGAEA.742579, (Rohardt, 2010),
- 1990. https://doi.org/10.1594/PANGAEA.527593, (Østerhus, 2006b),
- 1995. https://doi.org/10.1594/PANGAEA.742581, (Schröder, 2010),
- 1998. https://doi.org/10.1594/PANGAEA.527755, (Jenkins, 2006),
- 1999. https://doi.org/10.1594/PANGAEA.735530, (Rohardt & Harms, 2010),
- 2003. data from cruise ES006 (2003) are not searchable but available from BODC (https://www.bodc.ac.uk) on request (accession number BAS220012),
- 2009. https://doi.org/10.1594/PANGAEA.854148, (Nicholls & Fer, 2015),
- 2013. https://doi.org/10.1594/PANGAEA.846962, (Darelius & Fer, 2015),
- 2014. https://doi.org/10.1594/PANGAEA.833299, (Schröder & Wisotzki, 2014),
- 2016. https://doi.org/10.1594/PANGAEA.859040, (Schröder et al., 2016),
- 2017. https://doi.org/10.17882/54012 (Sallée, 2018),
- 2018. https://doi.org/10.1594/PANGAEA.897280, (Janout et al., 2019),
- 2021. https://doi.org/10.1594/PANGAEA.957614, (Tippenhauer et al., 2023).

The float data are available at https://doi.org/10.5281/zenodo.10353500 (F_{CS} as float 12684; F_{ST} as float 12682; F_{Sill} as float 12703) (Sallée, 2023). The hourly sea ice concentration and wind data from ERA5 reanalysis (Hersbach et al., 2018) were downloaded from https://cds.climate.copernicus.eu/datasets/reanalysis-era5-single-levels?tab=download (accessed on 26 October 2022) and the sea ice drift data from NSIDC (Tschudi et al., 2019) were downloaded from https://nsidc.org/data/nsidc-0116/versions/4#anchor-data-access-tools (accessed on 3 November 2022). The products for geostrophic velocities from altimetry data used for comparison were processed by SSALTO/DUACS (https://doi.org/10.24400/527896/a01-2022.010 version 2.0) and distributed by AVISO+ (https://www.aviso.altimetry.fr) with support from CNES, and are based on Auger et al. (2021).

Acknowledgments

This study receives funding from the European Union's Horizon 2020 research and innovation program under grant agreement N° 821001 (SO-CHIC), and N°820575 (TiPACCs) and from ESA via the SO-ICE project (AO/1–10461/20/I-NB). The authors would like to express their gratitude to the officers and crews of the RRS James Clark Ross (for the WAPITI cruise JC16004) and the RV Polarstern (for the COSMUS cruise PS124). The slope moorings and ED were funded through the Norwegian Research Council, project numbers 267660 and 328941. The authors would also like to thank two anonymous reviewers for their useful comments and suggestions.

References

Adusumilli, S., Fricker, H. A., Medley, B., Padman, L., & Siegfried, M. R. (2020). Interannual variations in meltwater input to the Southern Ocean from Antarctic ice shelves. *Nature Geoscience*, *13*(9), 616–620. https://doi.org/10.1038/s41561-020-0616-z

Arndt, J. E., Schenke, H. W., Jakobsson, M., Nitsche, F. O., Buys, G., Goleby, B., et al. (2013). The International Bathymetric Chart of the Southern Ocean (IBCSO) version 1.0—a new bathymetric compilation covering Circum-Antarctic waters. *Geophysical Research Letters*, *40*(12), 3111–3117. https://doi.org/10.1002/grl.50413

Årthun, M., Nicholls, K. W., Makinson, K., Fedak, M. A., & Boehme, L. (2012). Seasonal inflow of warm water onto the Southern Weddell Sea continental shelf, Antarctica. *Geophysical Research Letters*, *39*(17), L17601. https://doi.org/10.1029/2012GL052856

Auger, M., Prandi, P., & Sallée, J. B. (2021). Daily southern ocean sea level anomaly and geostrophic currents from multimission altimetry [Dataset]. *SEANOE*, 2013–2019. https://doi.org/10.17882/81032

Auger, M., Prandi, P., & Sallée, J.-B. (2022). Southern ocean sea level anomaly in the sea ice-covered sector from multimission satellite observations. *Scientific Data*, *9*(1), 70. https://doi.org/10.1038/s41597-022-01166-z

Daae, K., Darelius, E., Fer, I., Østerhus, S., & Ryan, S. (2018). Wind stress mediated variability of the Filchner Trough overflow, Weddell Sea. *Journal of Geophysical Research: Oceans*, *123*(5), 3186–3203. https://doi.org/10.1002/2017JC013579

Daae, K., Hattermann, T., Darelius, E., Mueller, R. D., Naughten, K. A., Timmermann, R., & Hellmer, H. H. (2020). Necessary conditions for warm inflow toward the Filchner ice shelf, Weddell Sea. *Geophysical Research Letters*, *47*(22), e2020GL089237. https://doi.org/10.1029/2020GL089237

Darelius, E., Daae, K., Dundas, V., Fer, I., Hellmer, H. H., Janout, M., et al. (2023). Observational evidence for on-shelf heat transport driven by dense water export in the Weddell Sea. *Nature Communications*, *14*(1), 1022. https://doi.org/10.1038/s41467-023-36580-3

Darelius, E., Dundas, V., Janout, M., & Tippenhauer, S. (2023). Sudden, local temperature increase above the continental slope in the southern Weddell Sea, Antarctica. *Ocean Science*, *19*(3), 671–683. https://doi.org/10.5194/os-19-671-2023

Darelius, E., & Fer, I. (2015). Physical oceanography from CTD in the Filchner depression (Weddell Sea, Antarctica) during Ernest Shackleton cruise ES060 [Dataset]. *Pangaea*. https://doi.org/10.1594/PANGAEA.846962

Darelius, E., Fer, I., Janout, M., Daae, K., & Steiger, N. (2024). Observations of the Antarctic slope current in the Southeastern Weddell sea: A bottom-enhanced current and its seasonal variability. *Journal of Geophysical Research: Oceans*, *129*(6), e2023JC020666. https://doi.org/10.1029/2023JC020666

Darelius, E., Fer, I., & Nicholls, K. W. (2016). Observed vulnerability of Filchner-Ronne Ice Shelf to wind-driven inflow of warm deep water. *Nature Communications*, *7*(12300), 1–7. https://doi.org/10.1038/ncomms12300

Darelius, E., Janout, M. A., Fer, I., & Sallée, J.-B. (2023). Physical oceanography and current velocity data from mooring M3 on the upper continental slope, east of Filchner Trough, February 2017 – February 2021 [Dataset]. *PANGAEA*. https://doi.org/10.1594/PANGAEA.962043

Darelius, E., Janout, M. A., Fer, I., & Sallée, J.-B. (2024). Physical oceanography and current velocity data from mooring M6 on the upper continental slope, east of Filchner Trough, February 2017 – February 2021 [Dataset]. *PANGAEA*. https://doi.org/10.1594/PANGAEA.964715

Darelius, E., Makinson, K., Daae, K., Fer, I., Holland, P. R., & Nicholls, K. W. (2014). Hydrography and circulation in the Filchner depression, Weddell Sea, Antarctica. *Journal of Geophysical Research: Oceans*, *119*(9), 5797–5814. https://doi.org/10.1002/2014JC010225

Darelius, E., Strand, K. O., Østerhus, S., Gammeslrød, T., Årthun, M., & Fer, I. (2014). On the seasonal signal of the Filchner overflow, Weddell Sea, Antarctica. *Journal of Physical Oceanography*, *44*(4), 1230–1243. https://doi.org/10.1175/JPO-D-13-0180.1

Darelius, E., & Wåhlin, A. (2007). Downward flow of dense water leaning on a submarine ridge. *Deep Sea Research Part I: Oceanographic Research Papers*, *54*(7), 1173–1188. https://doi.org/10.1016/j.dsr.2007.04.007

Davis, P. E. D., Jenkins, A., Nicholls, K. W., Dutrieux, P., Schröder, M., Janout, M. A., et al. (2022). Observations of modified warm deep water beneath Ronne ice shelf, Antarctica, from an autonomous underwater vehicle. *Journal of Geophysical Research: Oceans*, *127*(11), e2022JC019103. https://doi.org/10.1029/2022JC019103

Dotto, T. S., Naveira Garabato, A., Bacon, S., Tsamados, M., Holland, P. R., Hooley, J., et al. (2018). Variability of the Ross gyre, Southern Ocean: Drivers and responses revealed by satellite altimetry. *Geophysical Research Letters*, *45*(12), 6195–6204. https://doi.org/10.1029/2018GL078607

Eayrs, C., Li, X., Raphael, M. N., & Holland, D. M. (2021). Rapid decline in Antarctic sea ice in recent years hints at future change. *Nature Geoscience*, *14*(7), 460–464. https://doi.org/10.1038/s41561-021-00768-3

Foldvik, A., Gammelsrød, T., Øterhus, S., Fahrbach, E., Rohardt, G., Schröder, M., et al. (2004). Ice shelf water overflow and bottom water formation in the southern Weddell Sea. *Journal of Geophysical Research*, *109*(C02015), 1–15. https://doi.org/10.1029/2003jc002008

Fox, A. J., Paul, A., & Cooper, R. (1994). Measured properties of the Antarctic ice sheet derived from the SCAR Antarctic digital database. *Polar Record*, *30*(174), 201–206. https://doi.org/10.1017/S0032247400024268

Fretwell, P., Pritchard, H. D., Vaughan, D. G., Bamber, J. L., Barrand, N. E., Bell, R., et al. (2013). Bedmap2: Improved ice bed, surface and thickness datasets for Antarctica. *The Cryosphere*, *7*(1), 375–393. https://doi.org/10.5194/tc-7-375-2013

Hattermann, T. (2018). Antarctic thermocline dynamics along a narrow shelf with easterly winds. *Journal of Physical Oceanography*, *48*(10), 2419–2443. https://doi.org/10.1175/JPO-D-18-0064.1

Hattermann, T., Nicholls, K. W., Hellmer, H. H., Davis, P. E., Janout, M. A., Østerhus, S., et al. (2021). Observed interannual changes beneath Filchner-Ronne Ice Shelf linked to large-scale atmospheric circulation. *Nature Communications*, *12*(1), 2961. https://doi.org/10.1038/s41467-021-23131-x

Hellmer, H. H., & Holtappels, M. (2021). The expedition PS124 of the research vessel POLARSTERN to the southern Weddell Sea in 2021. *Berichte zur Polar- und Meeresforschung = Reports on Polar and Marine Research*, *755*, 237. https://doi.org/10.48433/BzPM_0755_2021

Hellmer, H. H., Kauker, F., Timmermann, R., Determann, J., & Rae, J. (2012). Twenty-first-century warming of a large Antarctic ice-shelf cavity by a redirected coastal current. *Nature*, *485*(7397), 225–228. https://doi.org/10.1038/nature11064

Hellmer, H. H., Kauker, F., Timmermann, R., & Hattermann, T. (2017). The fate of the southern Weddell Sea continental shelf in a warming climate. *Journal of Climate*, *30*(12), 4337–4350. https://doi.org/10.1175/JCLI-D-16-0420.1

Hersbach, H., Bell, B., Berrisford, P., Biavati, G., Horányi, A., Muñoz Sabater, J., et al. (2018). ERA5 hourly data on single levels from 1979 to present [Dataset]. *Copernicus Climate Change Service (C3S) Climate Data Store (CDS)*. https://doi.org/10.24381/cds.adbb2d47

Jacobs, S. S., Helmer, H. H., Doake, C. S., Jenkins, A., & Frolich, R. M. (1992). Melting of ice shelves and the mass balance of Antarctica. *Journal of Glaciology*, *38*(130), 375–387. https://doi.org/10.1017/S0022143000002252

Janout, M. A., Hellmer, H. H., Hattermann, T., Huhn, O., Sültenfuss, J., Østerhus, S., et al. (2021). FRIS revisited in 2018: On the circulation and water masses at the Filchner and Ronne ice shelves in the southern Weddell Sea. *Journal of Geophysical Research: Oceans*, *126*(6), e2021JC017269. https://doi.org/10.1029/2021JC017269

Janout, M. A., Hellmer, H. H., & Monsees, M. (2022). Raw data of physical oceanography and current velocity data from moorings AWI252-3, AWI253-3 and AWI254-3 in Filchner Trough, February 2018 – March 2021 [Dataset]. *PANGAEA*. https://doi.org/10.1594/PANGAEA.944430

Janout, M. A., Hellmer, H. H., Schröder, M., & Wisotzki, A. (2019). Physical oceanography during POLARSTERN cruise PS111 (ANT-XXXIII/2) [Dataset]. *PANGAEA*. https://doi.org/10.1594/PANGAEA.897280

Jenkins, A. (2006). Physical oceanography during cruise ROPEX at CTD station ROPEX_112-1 [Dataset]. *PANGAEA*. https://doi.org/10.1594/PANGAEA.527755

Lauber, J., de Steur, L., Hattermann, T., & Darelius, E. (2024). Observed seasonal evolution of the Antarctic slope current system off the coast of Dronning Maud land, east Antarctica. *Journal of Geophysical Research: Oceans*, *129*(4), e2023JC020540. https://doi.org/10.1029/2023JC020540

Lauber, J., Hattermann, T., De Steur, L., Darelius, E., Auger, M., Nøst, O. A., & Moholdt, G. (2023). Warming beneath an East Antarctic ice shelf due to increased subpolar westerlies and reduced sea ice. *Nature Geoscience*, *16*(10), 877–885. https://doi.org/10.1038/s41561-023-01273-5

Lauber, J., Hattermann, T., de Steur, L., Darelius, E., & Fransson, A. (2024). Hydrography and circulation below Fimbulisen ice shelf, east Antarctica, from 12 years of moored observations. *EGUsphere*, *2024*, 1–38. https://doi.org/10.5194/egusphere-2024-904

Martin, T., Tsamados, M., Schroeder, D., & Feltham, D. L. (2016). The impact of variable sea ice roughness on changes in arctic ocean surface stress: A model study. *Journal of Geophysical Research: Oceans*, *121*(3), 1931–1952. https://doi.org/10.1002/2015JC011186

McDougall, T., & Barker, P. (2011). Getting started with teos-10 and the Gibbs Seawater (GSW) oceanographic toolbox. *SCOR/IAPSO WG*, *127*, 1–28.

Moholdt, G., Padman, L., & Fricker, H. A. (2014). Basal mass budget of Ross and Filchner-Ronne ice shelves, Antarctica, derived from Lagrangian analysis of ICESat altimetry. *Journal of Geophysical Research: Earth Surface*, *119*(11), 2361–2380. https://doi.org/10.1002/2014JF003171

Morrison, A. K., Hogg, A. M., England, M. H., & Spence, P. (2020). Warm circumpolar deep water transport toward Antarctica driven by local dense water export in canyons. *Science Advances*, *6*(18), eaav2516. https://doi.org/10.1126/sciadv.aav2516

Nicholls, K. W., Abrahamsen, E. P., Heywood, K. J., Stansfield, K., & Østerhus, S. (2008). High-latitude oceanography using the Autosub autonomous underwater vehicle. *Limnology & Oceanography*, *53*(5), 2309–2320. https://doi.org/10.4319/lo.2008.53.5_part_2.2309

Nicholls, K. W., & Fer, I. (2015). Physical oceanography from CTD in the Weddell Sea, Antarctica, during the RRS Ernest Shackleton cruise ES033 [Dataset]. *PANGAEA*. https://doi.org/10.1594/PANGAEA.854148

Nicholls, K. W., Østerhus, S., Makinson, K., Gammelsrød, T., & Fahrbach, E. (2009). Ice-ocean processes over the continental shelf of the southern Weddell Sea, Antarctica: A review. *Reviews of Geophysics*, *47*(3), RG3003. https://doi.org/10.1029/2007RG000250

Nissen, C., Timmermann, R., Hoppema, M., Gürses, O., & Hauck, J. (2022). Abruptly attenuated carbon sequestration with Weddell Sea dense waters by 2100. *Nature Communications*, *13*(1), 3402. https://doi.org/10.1038/s41467-022-30671-3

Núñez-Riboni, I., & Fahrbach, E. (2009). Seasonal variability of the Antarctic coastal current and its driving mechanisms in the Weddell Sea. *Deep-Sea Research Part I Oceanographic Research Papers*, *56*(11), 1927–1941. https://doi.org/10.1016/j.dsr.2009.06.005

Østerhus, S. (2006a). Physical oceanography during ANDENES cruise NARE85 [Dataset]. *PANGAEA*. https://doi.org/10.1594/PANGAEA.527497

Østerhus, S. (2006b). Physical oceanography during ANDENES cruise NARE90 [Dataset]. *PANGAEA*. https://doi.org/10.1594/PANGAEA.527593

Østerhus, S. (2006c). Physical oceanography during POLARSIRKEL cruise NARE79 [Dataset]. *PANGAEA*. https://doi.org/10.1594/PANGAEA.527410

Østerhus, S. (2010). Physical oceanography during POLARSTERN cruise ANT-V/4 [Dataset]. *PANGAEA*. https://doi.org/10.1594/PANGAEA.734988

Pritchard, H., Ligtenberg, S., Fricker, H., Vaughan, D., van den Broeke, M., & Padman, L. (2012). Antarctic ice-sheet loss driven by basal melting of ice shelves. *Nature*, *484*(7395), 502–505. https://doi.org/10.1038/nature10968

Rignot, E., Jacobs, S., Mouginot, J., & Scheuchl, B. (2013). Ice-shelf melting around Antarctica. *Science*, *341*(6143), 266–270. https://doi.org/10.1126/science.1235798

Rohardt, G. (2010). Physical oceanography during POLARSTERN cruise ANT-VII/4 [Dataset]. *PANGAEA*. https://doi.org/10.1594/PANGAEA.742579

Rohardt, G., & Harms, S. (2010). Physical oceanography during POLARSTERN cruise ANT-XVI/2 [Dataset]. *PANGAEA*. https://doi.org/10.1594/PANGAEA.735530

Rossby, T., Dorson, D., & Fontaine, J. (1986). The rafos system. *Journal of Atmospheric and Oceanic Technology*, *3*(4), 672–679. https://doi.org/10.1175/1520-0426(1986)0032.0.CO;2

Ryan, S., Hattermann, T., Darelius, E., & Schröder, M. (2017). Seasonal cycle of hydrography on the eastern shelf of the Filchner Trough, Weddell Sea, Antarctica. *Journal of Geophysical Research: Oceans*, *122*(8), 6437–6453. https://doi.org/10.1002/2017JC012916

Ryan, S., Hellmer, H. H., Janout, M., Darelius, E., Vignes, L., & Schröder, M. (2020). Exceptionally warm and prolonged flow of warm deep water toward the Filchner-Ronne ice shelf in 2017. *Geophysical Research Letters*, *47*(13). https://doi.org/10.1029/2020GL088119

Ryan, S., Schröder, M., Huhn, O., & Timmermann, R. (2016). On the warm inflow at the eastern boundary of the Weddell Gyre. *Deep Sea Research Part I: Oceanographic Research Papers*, *107*, 70–81. https://doi.org/10.1016/j.dsr.2015.11.002

Sallée, J. B. (2018). Hydrological and current data for the Southern Weddell Sea, collected as part of the WAPITI oceanographic survey (JR16004) [Dataset]. *SEANOE*. https://doi.org/10.17882/54012

Sallée, J. B. (2023). Dataset of the paper: Subsurface floats in the Filchner Trough provide first direct under-ice tracks of eddies and circulation on shelf [Dataset]. *Zenodo*. https://doi.org/10.5281/zenodo.10353500

Sallée, J.-B., Vignes, L., Minière, A., Steiger, N., Pauthenet, E., Lourenco, A., et al. (2024). Subsurface floats in the Filchner Trough provide the first direct under-ice tracks of the circulation on shelf. *Ocean Science*, *20*(5), 1267–1280. https://doi.org/10.5194/os-20-1267-2024

Schröder, M. (2010). Physical oceanography during POLARSTERN cruise ANT-XII/3 [Dataset]. *PANGAEA*. https://doi.org/10.1594/PANGAEA.742581

Schröder, M. (2018). The expedition PS111 of the research vessel POLARSTERN to the southern Weddell Sea in 2018. *Berichte zur Polar- und Meeresforschung = Reports on Polar and Marine Research*, *718*, 161. https://doi.org/10.2312/BzPM_0718_2018

Schröder, M., Ryan, S., & Wisotzki, A. (2016). Physical oceanography during POLARSTERN cruise PS96 (ANT-XXXI/2 FROSN) [Dataset]. *PANGAEA*. https://doi.org/10.1594/PANGAEA.859040

Schröder, M., Ryan, S., & Wisotzki, A. (2017a). Physical oceanography and current meter data from mooring AWI252-1 [Dataset]. *PANGAEA*. https://doi.org/10.1594/PANGAEA.875931

Schröder, M., Ryan, S., & Wisotzki, A. (2017b). Physical oceanography and current meter data from mooring AWI253-1 [Dataset]. *PANGAEA*. https://doi.org/10.1594/PANGAEA.875932

Schröder, M., Ryan, S., & Wisotzki, A. (2017c). Physical oceanography and current meter data from mooring AWI254-1 [Dataset]. *PANGAEA*. https://doi.org/10.1594/PANGAEA.875933

Schröder, M., Ryan, S., & Wisotzki, A. (2019a). Physical oceanography and current meter data from mooring AWI252-2 [Dataset]. *PANGAEA*. https://doi.org/10.1594/PANGAEA.903104

Schröder, M., Ryan, S., & Wisotzki, A. (2019b). Physical oceanography and current meter data from mooring AWI253-2 [Dataset]. *PANGAEA*. https://doi.org/10.1594/PANGAEA.903315

Schröder, M., Ryan, S., & Wisotzki, A. (2019c). Physical oceanography and current meter data from mooring AWI254-2 [Dataset]. *PANGAEA*. https://doi.org/10.1594/PANGAEA.903317

Schröder, M., & Wisotzki, A. (2014). Physical oceanography during POLARSTERN cruise PS82 (ANT-XXIX/9) [Dataset]. *PANGAEA*. https://doi.org/10.1594/PANGAEA.833299

Sciremammano, F. J. (1979). A suggestion for the presentation of correlations and their significance levels. *Journal of Physical Oceanography*, *9*(6), 1273–1276. https://doi.org/10.1175/1520-0485(1979)009<1273:asftpo>2.0.co;2

Siahaan, A., Smith, R. S., Holland, P. R., Jenkins, A., Gregory, J. M., Lee, V., et al. (2022). The Antarctic contribution to 21st-century sea-level rise predicted by the UK Earth System Model with an interactive ice sheet. *The Cryosphere*, *16*(10), 4053–4086. https://doi.org/10.5194/tc-16-4053-2022

Steiger, N., & Sallée, J.-B. (2023). Hydrological and current velocity data from moorings P1, P2, P4, P5 and P6 in the Filchner Trough region in the southern Weddell Sea, February 2017 to March 2021 [Dataset]. *SEANOE*. https://doi.org/10.17882/100680

Stuecker, M. F., Bitz, C. M., & Armour, K. C. (2017). Conditions leading to the unprecedented low Antarctic sea ice extent during the 2016 austral spring season. *Geophysical Research Letters*, *44*(17), 9008–9019. https://doi.org/10.1002/2017GL074691

Sverdrup, H. (1953). The currents off the coast of queen maud land. *Norsk Geografisk Tidsskrift-Norwegian Journal of Geography*, *14*(1–4), 239–249. https://doi.org/10.1080/00291955308551737

Teske, V., Timmermann, R., & Semmler, T. (2024). Subsurface warming in the Antarctica's Weddell Sea can be avoided by reaching the 2c warming target. *Communications Earth & Environment*, *5*(1), 93. https://doi.org/10.1038/s43247-024-01238-5

Thoma, M., Determann, J., Grosfeld, K., Goeller, S., & Hellmer, H. H. (2015). Future sea-Level rise due to projected ocean warming beneath the filchner ronne ice shelf: A coupled model study. *Earth and Planetary Science Letters*, *431*, 217–224. https://doi.org/10.1016/j.epsl.2015.09.013

Tippenhauer, S., Janout, M. A., Schall, E., Timmermann, R., van Caspel, M., Vignes, L., et al. (2023). Physical oceanography based on ship CTD during RV POLARSTERN cruise PS124 [Dataset]. *PANGAEA*. https://doi.org/10.1594/PANGAEA.957614

Treasure, A. M., Roquet, F., Ansorge, I. J., Bester, M. N., Boehme, L., Bornemann, H., et al. (2017). Marine mammals exploring the oceans pole to pole: A review of the meop consortium. *Oceanography*, *30*(2), 132–138. https://doi.org/10.5670/oceanog.2017.234

Tschudi, M. A., Meier, W. N., Stewart, J. S., Fowler, C., & Maslanik, J. (2019). Polar pathfinder daily 25 km EASE-grid Sea ice motion vectors [Dataset]. *National snow and ice data center distributed active archive Center*. https://doi.org/10.5067/INAWUWO7QH7B

Vaňková, I., & Nicholls, K. W. (2022). Ocean variability beneath the filchner-ronne ice shelf inferred from basal melt rate time series. *Journal of Geophysical Research: Oceans*, *127*(10), e2022JC018879. https://doi.org/10.1029/2022JC018879